GEORG-AUGUST-UNIVERSITÄT
GÖTTINGEN

Fakultät für
Physik

Master's Thesis

Entwicklung des Detektorkontrollsystems für den ITk Outer Barrel Demonstrator des ATLAS Experiments

Development of the Detector Control System of the ITk Outer Barrel Demonstrator for the ATLAS Experiment

prepared by

Anne Gaa

from Speyer

at the II. Physikalischen Institut

Thesis number:	II.Physik-UniGö-MSc-2022/07
Thesis period:	18th November 2021 until 17th November 2022
First referee:	Prof. Dr. Stan Lai
Second referee:	Priv.Doz. Dr. Jörn Große-Knetter

Zusammenfassung

Im Zuge des High-Luminosity LHC-Upgrades wird der Inner Detector des ATLAS Experiments von einem reinen Siliziumdetektor, dem Inner Tracker (ITk) ersetzt, welcher den ITk Pixel und den ITk Strip Detektor enthält. Die Anforderungen an diesen neuen Detektor sind, eine bessere Leistung als der vorige zu haben bei der größeren Strahlenbelastung durch die erhöhte Luminosität. Dies gilt vor allem für den ITk Pixeldetektor, da dieser am nähesten zum Interaktionspunkt liegt. Der ITk Pixeldetektor wird eine neue Generation an Modulen besitzen, die auf Loaded Local Supports (LLS) in Serial Powering (SP) Ketten angeordnet sein werden. In der Outer Barrel (OB) Region des ITk Pixeldetektors gibt es zwei Arten von LLS, die Longerons und die geneigten Halbringe. Ein Demonstrator des ITk Pixeldetektors wurde für Systemtests gebaut in der finalen Prüfphase. Das Detektorkontrollsystem (DCS) ist ein Werkzeug zur Überwachung und Kontrolle des Demonstrators sowie des finalen Detektors. WinCC OA, eine SCADA Software, wird als Software des vernetzten Systems verwendet. Diese Masterarbeit stellt meine Arbeit vor, die im Zuge des ITk Pixel OB Demonstrator DCS ausgeführt wurde.

Abstract

In the scope of the High-Luminosity LHC-upgrade, the Inner Detector of the ATLAS experiment will be replaced by the all-silicon Inner Tracker (ITk), which includes the ITk Pixel and the ITk Strip detector. The requirements on the new detector will be to perform even better than its predecessor while withstanding the harsher radiation arising from the increased luminosity. This is especially true for the Pixel detector since it is closest to the interaction point. The ITk Pixel detector will have a new generation of modules mounted on the Loaded Local Supports (LLS) in Serial Powering (SP) chains. In the Outer Barrel (OB) of the ITk Pixel detector, there are two types of LLS, the longerons and the inclined half-rings. An ITk Pixel OB demonstrator was built for system tests in the final design review phase. The Detector Control System (DCS) is a tool for the monitoring and control of the demonstrator as well as the final detector. It uses WinCC OA, a SCADA software, in a distributed system. This master's thesis presents my work carried out in the scope of the ITk Pixel OB demonstrator DCS.

Contents

1 Introduction

Humans have the drive to explain the world around them. Particle physics takes this quest to the extreme in discovering the laws of nature on the most fundamental level possible. Matter was found to be made up of molecules, which were found to be made up of atoms, which were found to be made up of protons, neutrons and electrons. Afterwards came the development of modern high energy particle physics in the 20th century with particle colliders at energies high enough to investigate quarks, the constituents of neutrons and protons. It was found that the new fundamental constituents of matter were fermions, with particles called bosons as force carriers between particles. Fermions, bosons and their interactions in the form of the electromagnetic, weak and strong force are described in the quantum field theory of the Standard Model (SM) of particle physics.
At low energies, the SM is well understood. Particles of a high mass are unstable, since it is energetically advantageous for them to decay into lighter particles. The study of high mass particles requires large enough energies to produce them in a controlled environment. Such high mass particles can be produced in particle collisions, if the centre-of-mass energy is equal or higher than the energy equivalent to the particle mass.
Modern high energy physicists accelerate particles and collide them in detector experiments in order the study the properties of the collision products. These detectors are highly complex, with collaborations of physicists dedicated to their development, maintenance, and the analysis of the acquired data. One such experiment is the ATLAS detector [1] at the Large Hadron Collider [2] at CERN, the European Organization for Nuclear Research in Geneva. The ATLAS collaboration consists of over 3000 physicists from over 180 different institutions. The ATLAS detector and the CMS detector [3] are the two general-purpose experiments at the Large Hadron Collider. The experimental discovery of the Higgs boson by these two collaborations in 2012 [4, 5] is one of the most important achievements of modern particle physics.
New parts of the ATLAS detector are in development in preparation for the High-Luminosity LHC upgrade. The Inner Detector of the ATLAS detector will be replaced by the all-silicon Inner Tracker [6]. The Inner Tracker (ITk) is in the phase of its final design review, with different prototypes such as the Outer Barrel demonstrator located in the SR1

lab at CERN. An important tool for the monitoring and control of the final detector is the Detector Control System. The Detector Control System is also in the process of being upgraded, with different versions for the system tests of the Inner Tracker demonstrators. During my master's thesis, I worked on the Detector Control (DCS) for the Outer Barrel demonstrator of the ITk.
Chapter 2 will give an overview of the background information necessary for my projects. It contains a short introduction of the Standard Model, the Large Hadron Collider, the ATLAS experiment, the High-Luminosity Large Hadron Collider upgrade, and the Inner Tracker with the Outer Barrel demonstrator. Chapter 3 will explain the Detector Control System, both in general for the ATLAS experiment and more specifically for the system tests of the Outer Barrel demonstrator.
In Chapter 4, I will present the monitoring panels I created for the temperature and voltage monitoring of the modules mounted on the support structures of the ITk. There are two types of local support structures, longerons and half-rings. Both have their own type of monitoring panel. I also implemented the archiving of monitored data in the Outer Barrel demonstrator DCS. This is presented in Chapter 5. The procedure of archiving data with the respective configuration is shown as well as the different panels I created to facilitate this process. Lastly, I implemented several calibrations for the voltage and temperature monitoring in the DCS of the Outer Barrel demonstrator. They are presented in Chapter 6. These calibrations include a new conversion for temperature monitoring via temperature-dependent resistances and correction for the conversion of analog to digital signals. Parts of these calibrations are based on climate chamber measurements I conducted in the SR1 lab at CERN. In Chapter 7, the results of my work are summarised.

2 The LHC and the ATLAS Experiment

2.1 The Standard Model of Particle Physics

The theoretical framework of particle physics is provided by the Standard Model [7–9] of particle physics. It is a theoretical model of the particles and their interactions and has been shown to yield accurate experimental predictions. The particles in the SM are categorized into fermions, particles with a spin of $\frac{1}{2}$, and bosons, with integer spins. All elementary particles of the SM can be seen in Figure 2.1. Each particle has a corresponding anti-particle in the SM with the same internal quantum numbers but opposite electric charge. The particle interactions included in the theoretical framework of the SM are the weak, strong and electromagnetic interaction.
The fermions are themselves classified into quarks and leptons. Quarks occur in the flavours of up-type quarks u, c, t with a charge of $+\frac{2}{3}e$ and down-type quarks d, s, b with a charge of $-\frac{1}{3}e$. For the three generations of quarks, only the first one is stable, since the other two are progressively heavier and therefore it is energetically favourable to decay into the lighter particles. Quarks, along with gluons, are the only fundamental particles that carry a colour charge, which is a prerequisite for interacting via the strong force.
The leptons, as the second type of fermions also occur in three generations of progressively heavier particles. The charged leptons e^-, μ^-, τ^- have a charge of $-e$, while the lepton neutrinos ν_e, ν_μ, ν_τ have a charge of 0.
The bosons consist of the massless photon (γ) as the force carrier of the electromagnetic interaction, the massless gluon as the carrier of the strong interaction, the Z boson (Z^0) with a mass of 91.1 GeV as the carrier of the neutral weak current, the W ($W^\pm$) boson with a mass of 80.4 GeV as the carrier of the charged weak current, and the Higgs boson (H) with a mass of 125 GeV. The Higgs boson has a spin of 0 and is called a scalar boson while the other four have a spin of 1 and are called vector bosons.

The mathematics of particle interactions with electromagnetic, strong and weak forces can be represented in Feynman diagrams. A possible Feynman vertex for each force can

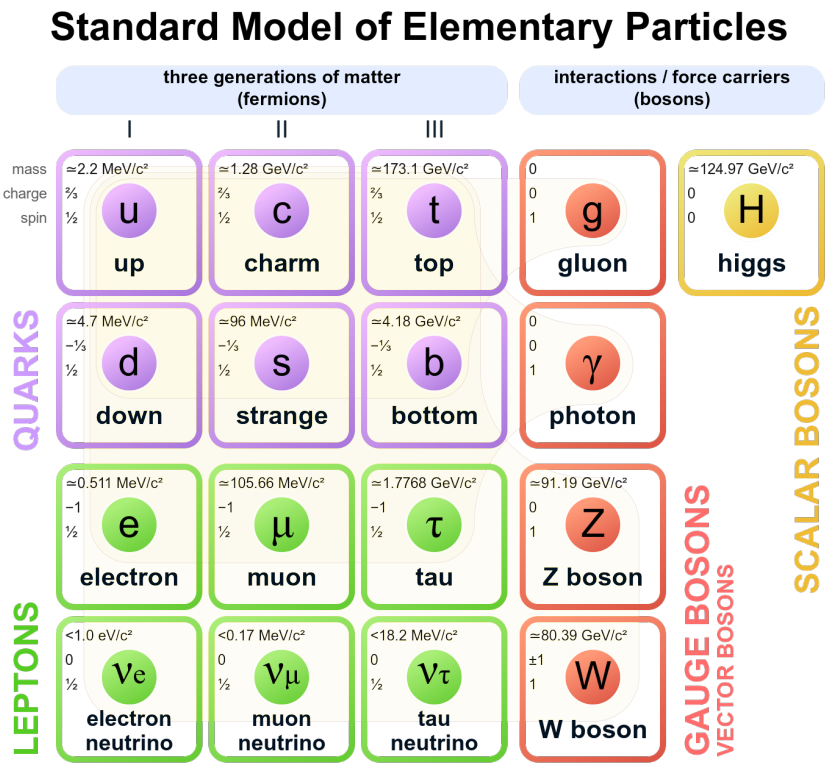

Figure 2.1: The particles in the SM with some of their properties, such as the mass or the electric charge. © Wikipedia

be seen in Fig. 2.2. The photon as the gauge boson of the electromagnetic interaction couples to all fermions except neutrinos, the gluon as the gauge boson of the strong force only to quarks, since it only couples to particles with colour charge, and the $W^{\pm}$ and Z^0 bosons couple to all fermions.

Colour charge in the model of the strong interaction is similar to electrical charge, only instead of plus and minus, there are the red (r), blue (b) and green (g) charges. Single quarks have one of the three possible colours as their colour charge, while anti-quarks have an anti-colour. Hadrons, composite particles that consist out of two or more quarks held together by gluons, must be colourless. The gluons always carry one colour and one anti-colour charge in eight possible combinations.

The neutral current Z^0 is not flavour-changing at leading order perturbation theory, meaning that it does not change a quark into a different quark or a lepton into a different lepton. The charged current $W^{\pm}$ is both always flavour-changing and the only interaction in the SM that changes the flavour of fermions. The probabilities of changing the flavour between different generations of quarks can be found in the Cabibbo-Kobayashi-Maskawa matrix [10], an $U(3)$ matrix with four free parameters that are determined experimentally.

The weak charged and neutral currents are also the only interactions in the SM to violate parity symmetry and charge-parity symmetry. In contrast to the gauge bosons of the other two interactions, the gauge bosons of the weak interaction have significant masses, which is explained in the SM with the Brout-Englert-Higgs mechanism [11–13].

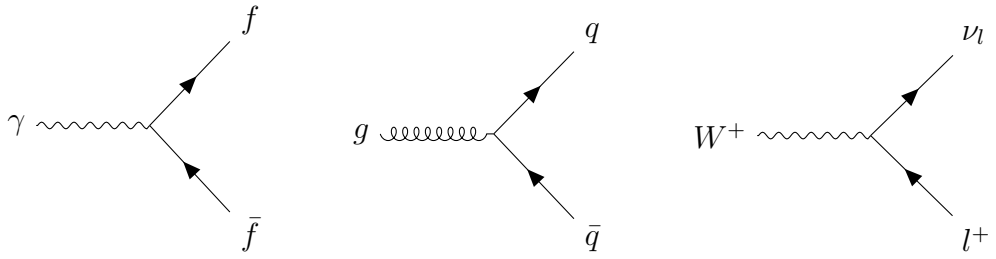

Figure 2.2: Feynman diagrams of examples for the electromagnetic, strong, and weak interaction

The SM can be modelled in terms of quantum field theory, where the three interactions are understood as local gauge symmetries. Quantum chromodynamics (QCD) [14, 15] has the $SU(3)_C$ group as its local gauge symmetry. The electromagnetic and the weak interaction are described in the quantum field theory of the SM as one interaction in the form of the electroweak unification [16–18]. At low energies the two interactions are observed separately from each other, with the photon as the gauge boson of the electromagnetic interaction and the Z^0 and $W^{\pm}$ as the gauge bosons of the weak interaction. At energies above the vacuum expectation value of the Higgs field of $v = 246$ GeV, the two neutral interactions merges into a single one. This gives an overall local gauge symmetry described by the $SU(2)_L \otimes U(1)_Y$ group, where the first term refers to weak isospin and the second one to hypercharge.

While it provides good predictions for experimental results, the SM is limited in its scope. It does not cover all particle interactions, since the gravitational force is not part of its model. One example for its limited scope is the phenomenon of dark matter [19]. Dark matter is assumed to exist due to observed rotational speeds of galaxies and anomalies in the measurements of gravitational density. The SM is not yet able to explain these experimental observations.

Another problem that the SM is not able to explain is the hierarchy problem [20]. The hierarchy problem is the name for the phenomenon of the gravitational force being 10^{24} times weaker than the weak interaction. This discrepancy between scales has no explanation in the SM. Tied into this problem is the previous expectation of the Higgs boson to have been heavier than the one discovered in 2012. The reason for that was that if the SM were valid up to extremely high mass scales, quantum loop corrections contributing to the

Higgs boson mass would have been very large. Since the Higgs boson was lighter than expected, the SM is therefore believed not to be valid to these high mass scales.
Further research in the field of high energy particle physics is necessary to find answers to these problems. One of the all-purpose experiments where this research is being conducted is the ATLAS experiment at CERN.

2.2 The Large Hadron Collider

The Large Hadron Collider (LHC) [2] is the world's largest and highest-energy particle accelerator and collider. The European Organization for Nuclear Reserach (CERN) built it from 1998 until 2008 in Geneva. It is located in an underground tunnel underneath the France-Switzerland border with a circumference of 27 km. It collides hadrons at a centre-of-mass collision energy as high as 13.6 TeV. The two general purpose experiments of the LHC are ATLAS and CMS. Aside from these experiments there is also LHCb for b-quark physics and ALICE for heavy ion experiments.
The accelerator chain of the LHC can be seen in Fig. 2.3. It starts with linear accelerator the Linac4 [21], which was put into operation in 2020. In Linac4, negative hydrogen ions are accelerated to an energy of 160 MeV in preparation of them entering the Proton Synchrotron Booster (PSB). There, the electrons are stripped from the hydrogen so only protons are left and accelerated to 2 GeV. Afterwards the protons are injected into the Proton Synchrotron (PS) and boosted up to 26 GeV, and in the last step before entering the LHC they are accelerated in the Super Proton Synchrotron (SPS) up to 450 GeV. The injection from the SPS into the LHC beamline happens at two points, where the clockwise and anti-clockwise circulating protons are injected, respectively.

In the four experiments along the LHC, protons from the clockwise and anti-clockwise beamline are collided. These collisions are called events or interactions. The rate of events generated by LHC collisions is given by:

$$\frac{\mathrm{d}N_{\text{event}}}{\mathrm{d}t} = L\sigma_{\text{event}}. \tag{2.1}$$

with the instantaneous luminosity L and cross-section of the underlying event σ_{event}. In order to obtain the total amount of events generated over a set time, we need to integrate Eq. 2.1, with the cross-section being independent of time:

$$N_{\text{event}} = \int L\mathrm{d}t\sigma_{\text{event}} = L_{\text{int}}\sigma_{\text{event}}. \tag{2.2}$$

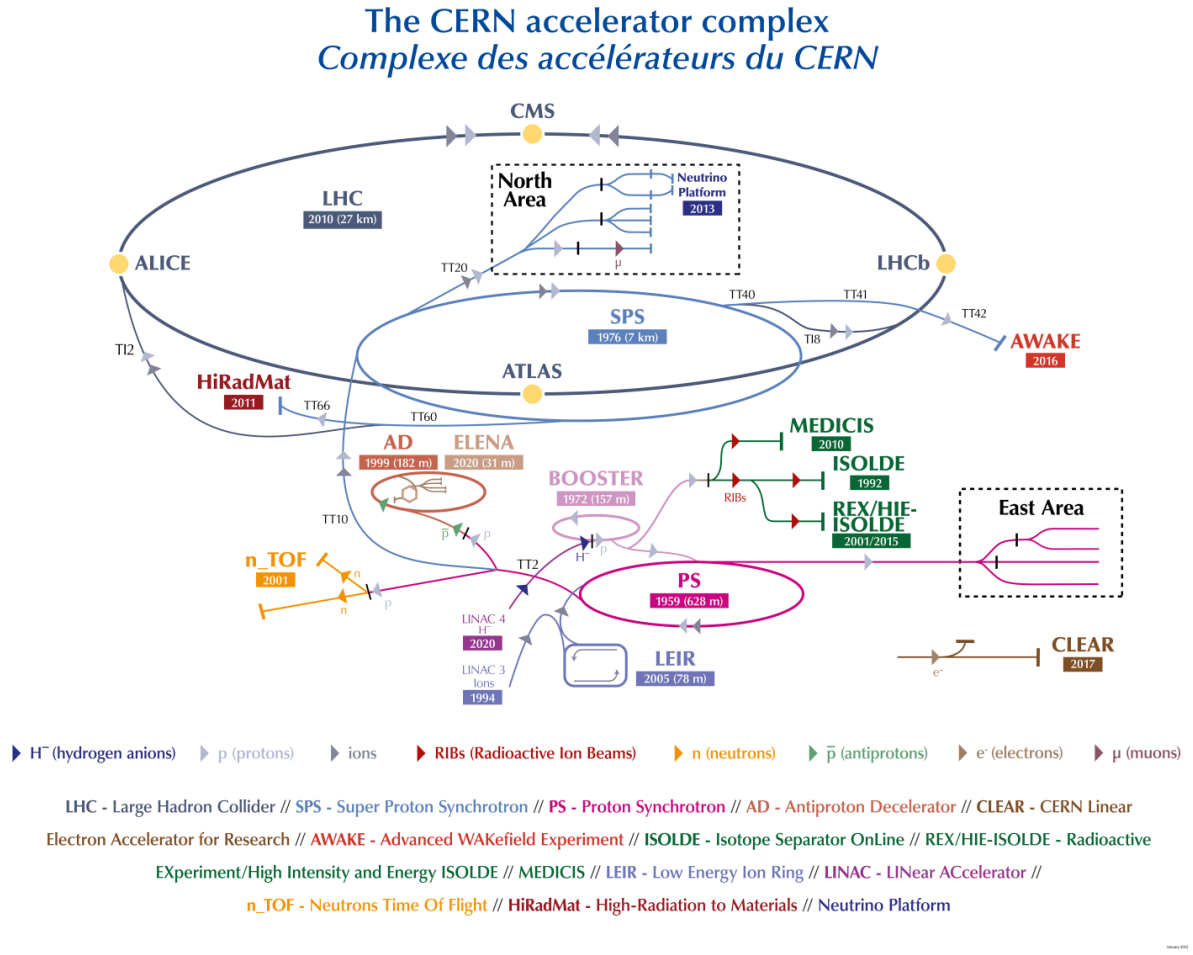

Figure 2.3: Layout of the LHC accelerator chain. © CERN

L_{int} is the integrated luminosity. The instantaneous luminosity of the LHC depends on the number of protons being collided. Protons are inserted in bunches of approximately $1.15 \cdot 10^{11}$ protons per bunch and there are 2808 bunches in the beamline of the LHC. This leads to a spacing of 25 ns between the crossing of two bunches at set points in the LHC. Data-taking takes place at the LHC over long periods of time, between which upgrades and maintenance work are done. Run 1 of the LHC started in March 2011 at a beam energy of 3.5 TeV, which was later increased to 4 TeV. The integrated luminosity of Run 1 was approximately 30 fb^{-1} when it ended in 2012. After the first Long Shutdown (LS), Run 2 took place from 2015 until 2018 at a beam energy of 6.5 TeV. In Run 2, the peak instantaneous luminosity of $2 \cdot 10^{34}$ $\text{cm}^{-2}\text{s}^{-1}$ was reached with an integrated luminosity of 190 fb^{-1}. Run 3 was started in 2022 at 6.5 TeV and is planned to last until 2024, with a predicted integrated luminosity of 350 fb^{-1} and a beam energy of 7 TeV.

2.3 The ATLAS Experiment

The ATLAS (A Toroidal LHC ApparatuS) experiment [1] is a general-purpose particle detector at the LHC at CERN. The experiment involves about 3000 physicists from over 180 different institutions. Its purpose is to observe high energy particles collided by the LHC in order to probe the SM of particle physics at new energy scales and search for new physics beyond the Standard Model. The ATLAS collaboration has made many important contributions to the field of particle physics, one of the most important being the experimental discovery of the Higgs boson together with CMS in 2012 [4, 5]. Its general layout with the main components can be seen in Fig. 2.4.

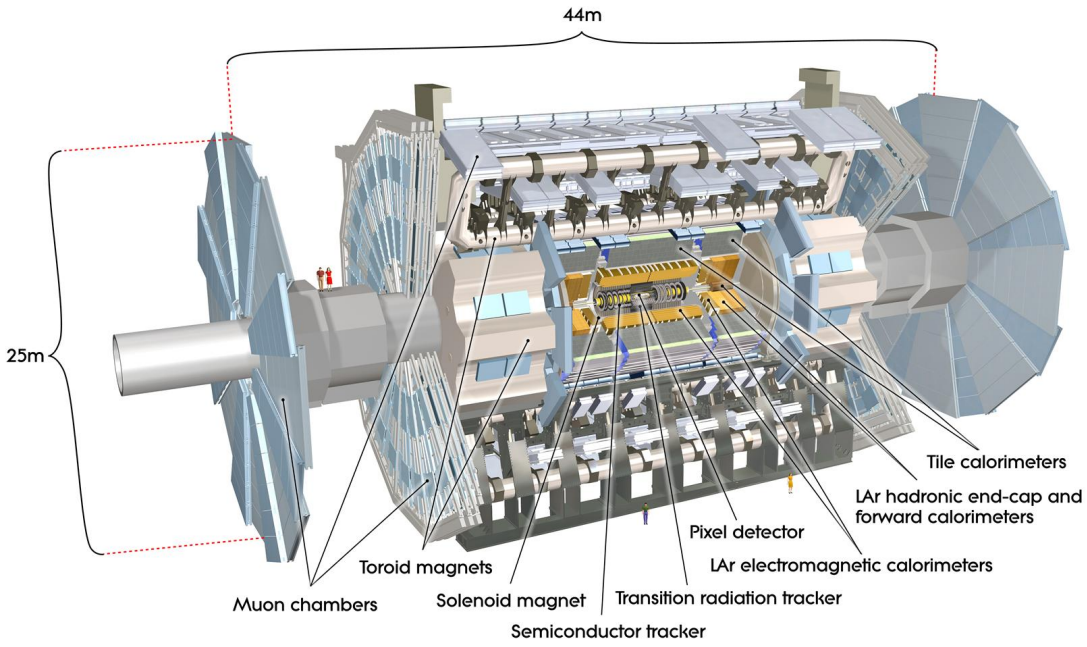

Figure 2.4: Layout of the ATLAS detector [1]

The ATLAS detector is 25 m high and 44 m long in the form of a cylinder that is forward-backward symmetric with respect to the collision point in its middle, where the two beamlines of the LHC cross. At its core is the inner detector, which is divided into the pixel detector, the semi-conductor tracker, the transition radiation tracker. Outside of the inner detector, the calorimeters are located, first the electromagnetic and then the hadronic one. The outer shell of the detector houses the magnet system and the muon spectrometer.

The beamline of the LHC is located along the z-axis, with the collision point as the origin

of the coordinate system. The positive x-axis points to the center of the LHC and the positive y-axis points upwards in a right-handed system. The coordinates can also be expressed in terms of cylindrical coordinates with the radius r, the azimuthal angle ϕ, the angle around the beam axis and the polar angle θ, the angle from the beam axis. The pseudorapidity $\eta = -\ln(\tan(\theta/2))$ is often used to describe the coverage of the detector.

Inner Detector The layout of the Inner Detector [1] of the ATLAS experiment can be seen in Fig. 2.5. Its subsystems are the pixel detector, the semi-conductor detector (SCT) and the transition radiation tracker (TRT). It provides pattern recognition, momentum resolution and primary as well as secondary vertex measurements for tracks of charged particles with a minimum transverse momentum p_T of 0.1 to 0.5 GeV. Its overall coverage is $|\eta| < 2.5$. The inner solenoid applies a magnetic field of $B = 2$ T, in which the ID is immersed, which directs charged particles onto a curved trajectory. From the direction and the radius of this trajectory, the mass and charge of particles can be inferred. The resolution of the transverse momentum of the Inner Detector is $\sigma_{p_T}/p_T = 0.04 \times p_T$ [GeV] [22].

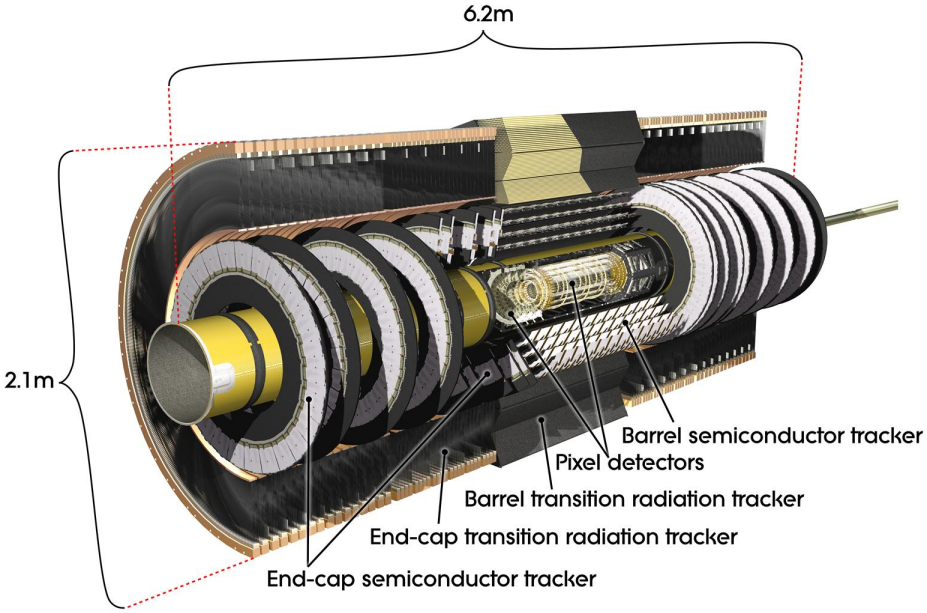

Figure 2.5: Layout of the ATLAS Inner Detector [1].

Directly around the collision point of the ATLAS detector is the pixel detector. It consists of three cylindrical layers and possesses a high granularity in order to allow high-resolution pattern recognition using space-points from its silicon sensors. The pixel detector was built with FE-I3 chips [23] readout chips with 2880 pixels per chip with an active area of 0.58 cm^2. This corresponds to a minimum pixel size of $50 \times 400 \mu$m^2 in

the R-$\phi \times z$ plane. 26 FE-I3 chips are grouped together in a module with 1744 modules overall. During the LS from 2012 until 2014, the innermost layer of the pixel detector up to a radius of 3.3 cm was replaced with the Insertable B-Layer (IBL) [24] in order to improve the performance of the tracking system after its decline due to radiation damage. With the IBL upgrade the Inner Detector contains over 92 million readout channels, which is more than half of the total readout channels of the ATLAS detector. It contains the newer generation of readout chips, the FE-I4 [25], with 26 880 pixels in an active area of 3.36 cm^2. The IBL consists of 14 carbon fibre staves with 32 FE-I4 chips each stave.
The SCT is located around the pixel detector. It is a silicon microstrip detector with four layers of radii from 299 mm to 514 mm in the barrel region and nine disks in each end-cap region. It has four rectangular silicon-strip sensors [26] grouped together in a module with a second pair of sensors glued back-to-back at a stereo angle of 40 mrad with 4088 modules overall. One module has 768 strips with each about 12 cm in length. The two silicon detectors are cooled down at -5 to -10°C in order to reduce thermal noise after radiation damage.
The outermost part of the inner detector is the TRT. It is made out of gaseous straw tubes interspersed with transition radiation material. It makes use of the phenomenon of transition radiation, which takes place when a charged particles propagates through a boundary between materials of different dielectric constants and emits radiation. The intensity of this radiation is proportional to the Lorentz factor $\gamma = \frac{E}{mc^2}$ of the particle. The TRT is especially suited to identifying electrons, since they tend to have high Lorentz factors due to their small mass.

Calorimetry The calorimetry of the ATLAS detector is located outside of the solenoidal magnet of the inner detector. Its layout can be seen in Fig. 2.6. Calorimeters measure the energy of particles in a destructive process, where the particles enter the calorimeter, initiate a particle shower and the energy of the shower particles is measured. The calorimeters of the ATLAS detector provide good containment for hadronic and electromagnetic showers due to their size. This means that only muons and neutrinos tend to leave the calorimeters and reach the outer parts of the detector.

The ATLAS calorimeter consists of the Electromagnetic Calorimeter (ECal) located just outside the inner detector, followed by the Hadronic Calorimeter (HCal). Both are sampling calorimeters with alternating layers of materials for absorption and detection. The calorimetry covers a range of $|\eta| < 4.9$. In the $0 < |\eta| < 2.5$ region, the granularity of the ECal is adjusted for precision measurements of electrons and photons. The rest of the calorimeter has a coarser granularity and is used for jet reconstruction and measurements of the missing transverse energy E_T^{miss}.

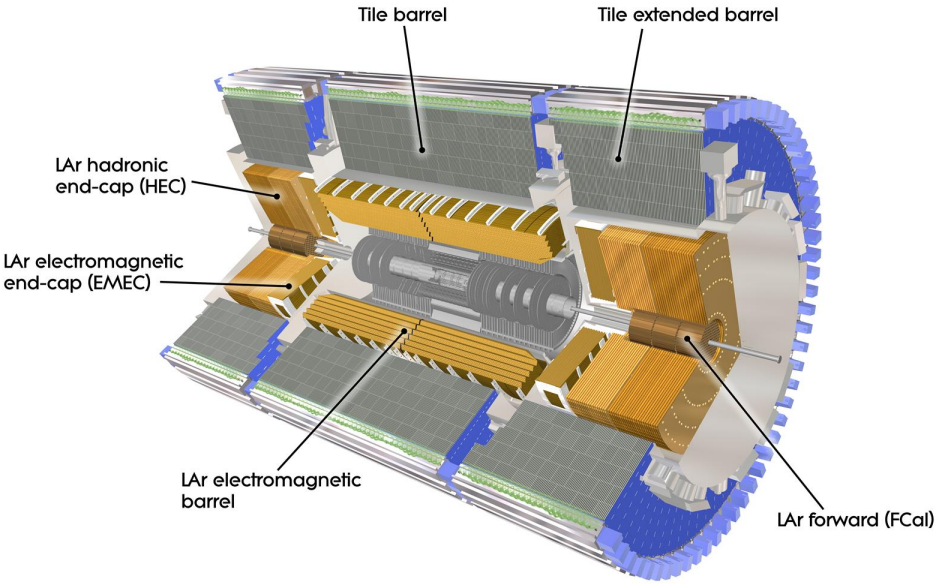

Figure 2.6: Layout of the ATLAS Calorimetry [1].

The ECal uses liquid argon (LAr) as the active material and lead as the absorbing material. Its accordion geometry provides complete coverage in the azimuthal angle ϕ without gaps. It covers a pseudorapidity range of $|\eta| < 3.2$ with an energy resolution of $\sigma_E/E = 10\%/\sqrt{E} \bigoplus 0.7\%$ [GeV] for electromagnetic showers.
The HCal consists of the Tile Calorimeter, divided into barrel and end-cap regions, the LAr hadronic end-cap calorimeter and the LAr forward calorimeter. The HCal uses steel as the absorber medium, with the active medium as scintillator tiles for the Tile Calorimeter and liquid argon for the LAr calorimeters. The Tile Calorimeter covers a range of $|\eta| < 1.7$ while the LAr end-caps cover $1.5 < |\eta| < 3.2$. Both have an energy resolution of $\sigma_E/E = 50\%/\sqrt{E} \bigoplus 3\%$ [GeV], with the resolution for the HCal being valid for pion showers. The LAr forward calorimeter covers a range of $3.1 < |\eta| < 4.9$ with an energy resolution of $\sigma_E/E = 100\%/\sqrt{E} \bigoplus 10\%$ [GeV].

Muon System The layout of the ATLAS muon system can be seen in Fig. 2.7. It is located in the outer part of the detector and detects charged particles exiting the calorimeter in a pseudorapidity range of $|\eta| < 2.7$. These particles are almost all muons, since other charged particles are absorbed by the calorimeters beforehand. With separate trigger and high-precision tracking chambers, the muon tracks are deflected in the large superconducting toroid magnets. The chambers in the barrel are arranged in three cylindrical shells around the beam at different radii, while the end-cap region chambers form wheels perpendicular to the beam axis. In the range of $|\eta| < 1.4$, the barrel toroid

provides magnetic bending with a magnetic field of 0.5 T for the central region and 1 T for the end-cap region. Between $1.6 < |\eta| < 2.7$, tracks are bent via the smaller end-cap magnets. In the transition region $1.4 < |\eta| < 1.6$, muons are magnetically deflected via a combination of barrel and end-cap magnets. This results in a magnetic field mostly orthogonal to the trajectory of the muons, while minimising the degradation of resolution arising from multiple scattering. The magnetic field forces muons onto curved trajectories, which are detected via Monitored Drift Tubes (MDTs). These tubes occur in higher granularities in the innermost plane over $2 < |\eta| < 2.7$ in order to withstand the high rate and background conditions.

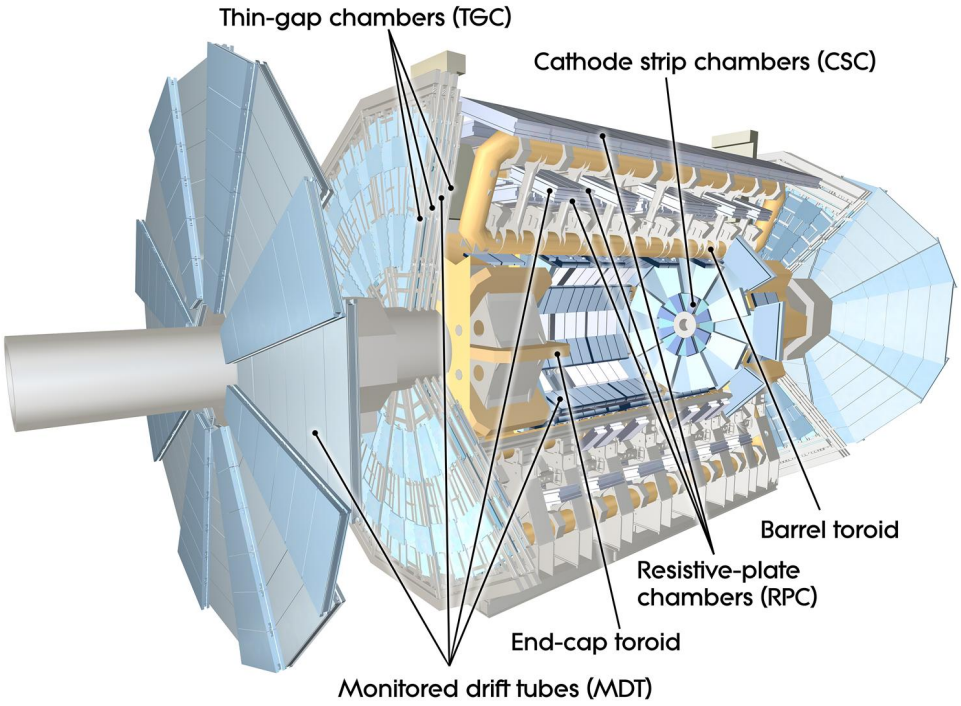

Figure 2.7: Layout of the ATLAS Muon System [1].

The high precision-tracking chambers are complemented by a trigger system that covers the pseudorapidity range of $|\eta| < 2.4$. The trigger chambers serve three purposes: providing bunch-crossing identification, providing well-defined p_T thresholds and measuring the muon coordinate in the orthogonal direction to the track as determined by the precision-tracking chambers.

In the LS before Run 3, the Small Wheels at the end-caps were upgraded to the New Small Wheels in preparation for the increased luminosity. The two 10 meter diameter wheels replace the first muon stations in the high-rapidity regions of ATLAS and will each cover more than 1200 m^2 of active area [27].

The relative p_T resolution of the muon system is approximately 10% for tracks with a

minimum p_T of 1 TeV.

Trigger System The ATLAS experiment employs a two-level trigger system to reduce the rate of recorded events [28]. Starting with a proton-proton interaction rate of 40 MHz due to the maximum instantaneous luminosity of 10^{34} $\mathrm{cm}^{-2}\mathrm{s}^{-1}$, the recorded collision data is reduced to an average rate of 1 kHz.

The Level-1 (L1) trigger is hardware based and uses custom electronics in order to trigger on information from the calorimeter and muon detectors. The L1 selects events by considering quantities such as the energy deposited in the calorimeter or the transverse momentum of a muon and reduces the accepted event rate down to 100 kHz. The second stage of the trigger, the High Level Trigger (HLT), is software-based. Fast trigger algorithms provide early rejection which is followed by more precise algorithms similar to offline reconstruction in order to make the final selection.

2.4 The High-Luminosity LHC Upgrade

The High-Luminosity LHC upgrade is currently in development [29]. This will improve the instantaneous luminosity of the LHC approximately by a factor of five and therefore greatly increase the data sample produced by the collider. Following five years of design study and R&D, ten further years of developments, prototyping, testing and implementation are planned. The current state of the schedule can be seen in Fig. 2.8. It can be seen that at the end of 2023, radiation damage limits Run 3 of the LHC. Starting in 2024 during the third long shutdown (LS3), the HL-LHC will be installed while other parts of ATLAS and CMS will be upgraded as well.

With this upgrade, the HL-LHC will produce data of up to an integrated luminosity of 4000 fb $^{-1}$ by 2038. The higher instantaneous luminosity means that the radiation damage will be higher. The upgraded detectors need to reflect that and are also required to perform at the same level or even better than before. Additionally, the amount of data accumulated necessitates an significantly larger bandwidth than before. This improvement in statistics will yield better precision measurements for known processes as well as give a higher chance to study rare processes that occur at the current centre-of-mass energy.

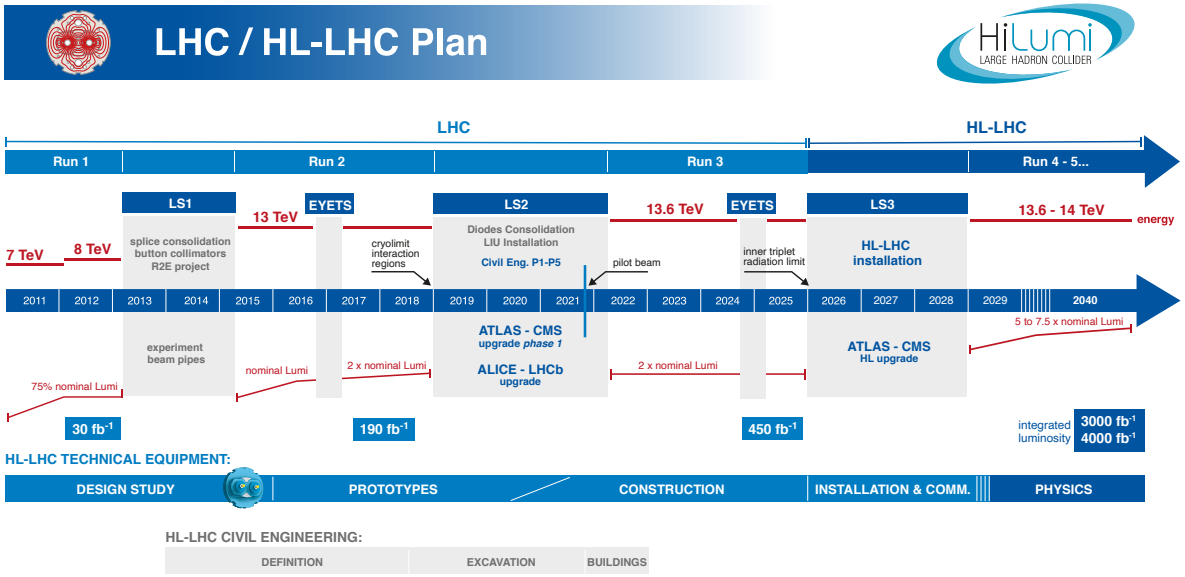

Figure 2.8: Schedule of the HL-LHC Upgrade, updated February 2022. [29]

2.5 The ATLAS Inner Tracker (ITk) Pixel Detector

The higher instantaneous luminosity provided by the HL-LHC upgrade means that the radiation damage to the detector will also increase. The detector needs to be able to withstand this for the duration of its operation time of more than ten years. This needs to be taken into account for the upgrades of the detectors themselves. Another criterion is that the tracking performance should be as good or better than before. For this, the current ATLAS inner detector will be replaced by a new all-silicon Inner Tracker (ITk)[30]. A schematic cross section of a quadrant of the ITk detector can be seen in Fig. 2.9 (a). It consists of two subsystems: the pixel detector [6] and the strip detector [31]. Fig. 2.9 (b) shows a cross section of a quadrant of the ITk pixel detector. It can be seen that the pixel system is itself divided into the three regions of the outer barrel (OB), the outer endcaps and the inner barrel and endcaps. The strip system will have a coverage up to an absolute pseudorapidity of $|\eta| = 2.7$ and the pixel system up to $|\eta| = 4$.

Supports structures of the ITk pixel detector need to be light, rigid and thermally conductive. Materials used include carbon fibre laminates, pyrolytic graphite and other carbon based composites. A small diameter titanium pipe is embedded in the structure for heat extraction via a CO_2 cooling system. The modules are then mounted on the local supports which are then called Loaded Local Supports (LLS).
The modules mounted on the support structures are arranged in serial powering (SP)

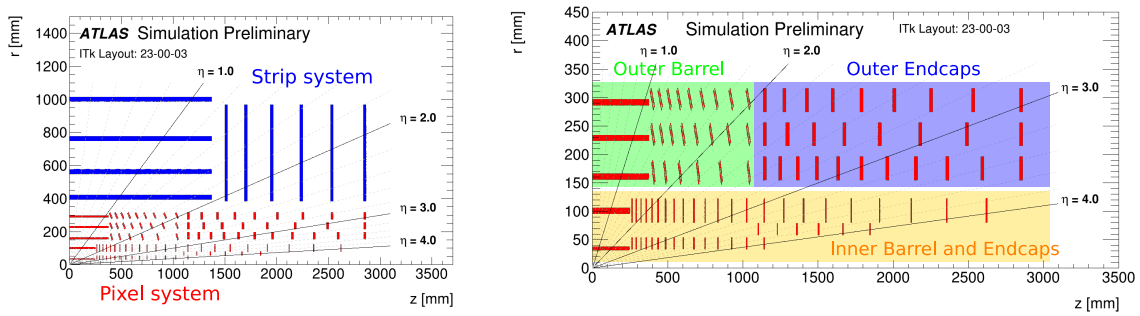

(a) *(b)*

Figure 2.9: a) Layout of a quadrant of the ITk detector with the strip system (blue) and the pixel system (red) and b) layout of the pixel system showing the three regions outer barrel (green), outer endcaps (blue) and inner barrel and endcaps (orange) [30].

chains of up to 14 modules supplied by a single current source. All sensors will be biased with the same high voltage (HV) of up to 200 V, while the modules will be operated with a low voltage (LV) of 1.2 V. Using SP chains reduces the material in a sensitive detector and reduces the number of cables necessary. Using this setup is challenging, as the modules will need to work with constant current input, and due to the nature of serial powering, the whole chain will be non-operational in the case of a single module failure.
The OB has two types of local supports. The first are longerons parallel to the beamline at different radii. As can be seen in Fig. 2.10, one longeron has four SP chains and is symmetric to the interaction point located at the middle of it.

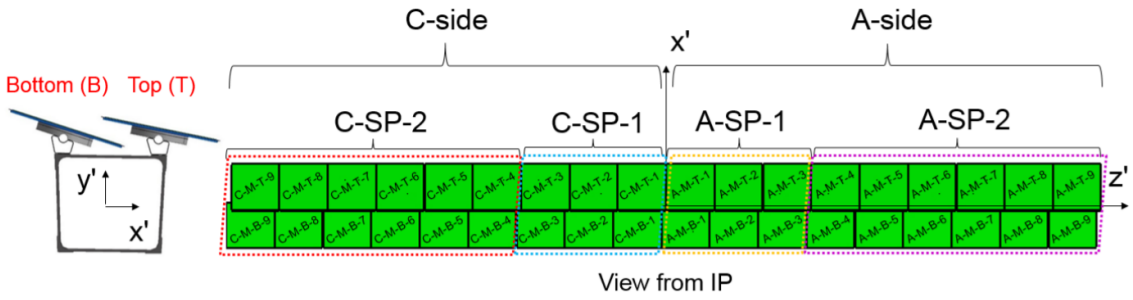

Figure 2.10: Definition of the modules in an OB longeron. The central SP chains feature six modules each, while the outer chains comprise twelve modules each [32].

The inclined half-rings are the second type of local support found in the OB. They have a coverage of $1 \leq |\eta| \leq 3$ and are inclined to the beam line at an angle of 56°. Half-rings have two SP chains with 8, 11 or 14 modules in layer 2, 3 or 4 respectively. A half-ring of

layer 2 can be seen in Fig. 2.11. In the half-rings, the module cells are soldered to the cooling pipe alternately on the front and back sides to achieve a double-sided cooling pipe.

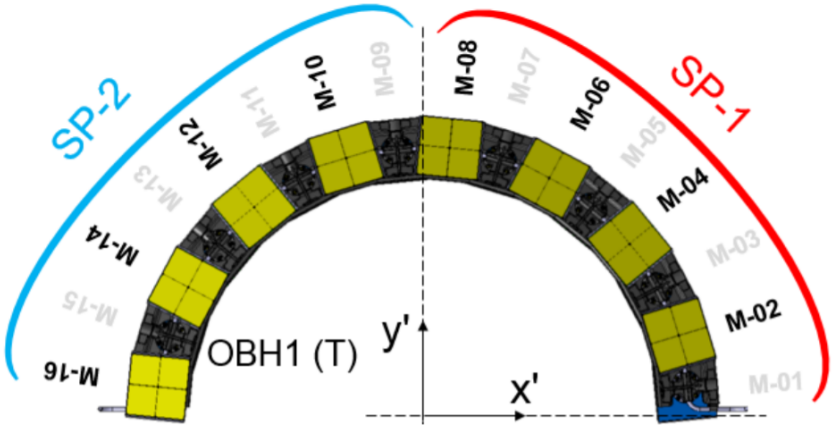

Figure 2.11: Definition of the modules in an OB inclined half-ring. Layers 2, 3 and 4 have respectively 8, 11 and 14 modules per SP chain, with each half-ring having two SP chains. The half-ring shown corresponds to layer 2 [32].

The three increasing layers of the OB region are called Layer 2, 3 and 4 in increasing radii from the beamline. Fig. 2.12 shows the coupling of the longerons to the cooling system in a cross section of the longerons. Sensors, readout chips, and the power supply structure are also mounted on the LLS.

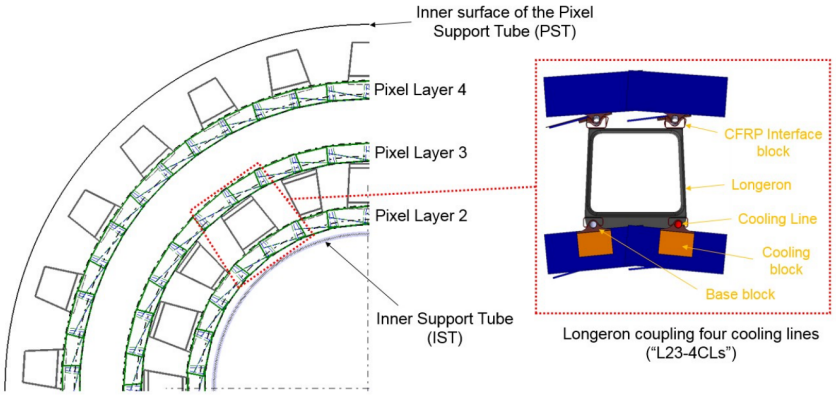

Figure 2.12: R-ϕ view of the three outer pixel barrel layers showing the cross section of the different longerons and the coupling to the cooling system [6].

2.6 The ITk Pixel Outer Barrel Demonstrator

To test the on-detector components, system tests for all three regions of the Pixel Detector are planned. In order to perform system tests of different subsystems of the ITk pixel detector, prototypes of these subsystems need to be built.
Any demonstrator of the ITk Pixel Outer Barrel (OB) needs to fulfill both the technical requirements of the pixel system in general from Ref. [33] and the more specific ones for the OB from Ref. [34]. The assembly of the OB demonstrator as a slice prototype is part of the design qualification. It is based on the geometry of layer 3 and is comprised of one longeron and two inclined half-rings with at least one SP chain each, so that both types of LLS are included in the design review.
In order to collect cables at relevant breakpoints, Patch Panels (PPs) are used. The first breakpoint is the PP0, where the electrical service from the modules comes in. The demonstrator will test the LLS with their corresponding PP0. Aside from this, it also includes representative sections from the global structures of intermediate supports, half-layer shells, service support shells and cooling pipe extensions. System tests on these systems seek to validate the entire service chain.
In the final design review, the OB demonstrator is populated with modules using the RD53A front-end chips [35]. The RD53A chip was developed with testing purposes for the development of the ITk Pixel detector and is not intended for the final experiment. The RD53A modules are half-sized demonstrator modules for evaluating three analogue front ends and two readout architectures. Based on the results of extensive testing of the RD53A modules, the ITkPixV1 modules [36], which are not yet ready for system tests, were developed for the final experiment.
An important tool in operating and validating the demonstrator is its Detector Control System. It monitors and controls the different subsystems and ensures their safe operation. An important part of the control system that ensures safety is the interlock. The interlock is hardware-based and independent of other systems, and can shut down necessary systems to avoid harm to people or detector parts.
The system test for the OB demonstrator should check the following [37]:

1. Verify that the interlock functions correctly
2. Verify the readout path
3. Verify the powering scheme (LV and HV)
4. Test the serial powering scheme
5. Test the modules

6. Validate the services
7. Check the detector control system
8. Run under realistic conditions
9. Check for cross talk between modules
10. Perform source tests, i.e. module tests with radiation, for signal generation

One system test will use the OB demonstrator built in SR1. A schematic view of the demonstrator can be seen in Fig. 2.13 and its technical details are described in Ref. [38]. In a first step, 27 RD53A modules with at least one full SP chain on each LLS will be mounted on the demonstrator, though the capacity for modules mounted on LLS is up to 40 modules and can be increased later on. Once ITkPixV1 modules become ready for testing, they can also be installed.
The electrical signal of the readout of the modules is converted into an optical signal via an optobox with optoboards, to take advantage of the speed with which optical signals can be transported. The monitoring of the module temperature and voltage is performed by a dedicated application-specific integrated circuit (ASIC) named MOPS (Monitoring of Pixel System) [39]. Each optobox and each SP chain will have one MOPS chip. The communication interface between the MOPS and the Detector Control System is the MOPSHUB. The MOPS are connected via CAN (Controller Area Network) bus with the CANopen protocol to MOPSHUB at PP3. The MOPS and MOPSHUB are able to read monitoring data independent of the data taking state of the detector and therefore provide good redundancy.

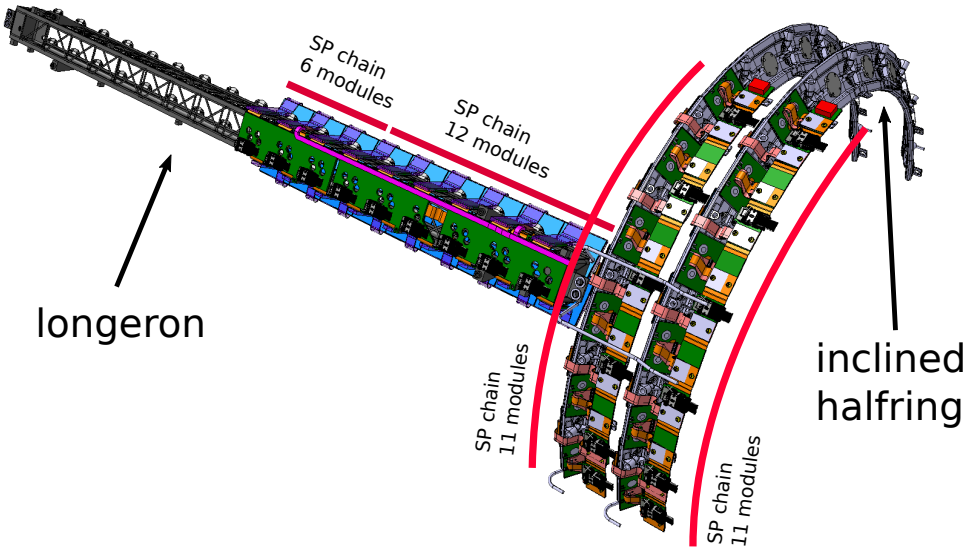

Figure 2.13: Rendering of the OB demonstrator with one longeron and two half-rings. The longeron will have two full SP chains with respectively 6 and 12 modules each while the half-rings will have one full SP chain each [38].

3 Detector Control System for ATLAS

The individual detector components as well as the experimental infrastructure of the ATLAS experiment are supervised by its Detector Control System (DCS). Next to supervision via operator commands, it reads, processes and archives the operational parameters of the detector, allows for error recognition and handling and manages the communication with external control systems, providing a synchronization mechanism with the data acquisition system of the detector. Due to the size of the ATLAS detector and the duration of its operation, standardization of hardware and software components is needed for an efficient development process and long-term maintainability of the DCS.
The DCS has several requirements. The detectors, subdetectors, subsystems etc. organized within its hierarchical structure have a certain level of operational independence. This must already be taken into account during the development process starting with small stand-alone systems for prototyping up to the final operation of the detector. Aside from the operational mode of data-taking, the maintenance and calibration modes also need to be supported. Another requirement is the long-term maintainability of hardware and software components and a high level of scalability, where small-scale demonstrators can easily be scaled up to the final detector. The ATLAS experiment is located 100m underground and its cavern is not accessible for persons to perform maintenance during data-taking periods due to the radiation-heavy environment. This means that the DCS must be fault-tolerant and allow for remote diagnostics of errors. Dependence on external services should be kept as minimal as possible [40].
The ATLAS DCS can be divided into the front-end (FE) equipment and the back-end (BE) systems. Communication between these is provided mostly via CAN with the CANopen protocol or via ethernet with the OPC UA protocol. The FE equipment consists of devices such as power supplies and sensors. Embedded Local Monitoring Boards (ELMB) [41] are multipurpose devices used for different FE control and monitoring tasks. The BE of the ATLAS DCS consists of the SCADA system WinCC OA. The framework of the DCS is encompassed by the Joint Controls Project (JCOP) [42], a collaboration between the

LHC experiments. Within it, standards for DCS hardware were established and control software has been chosen as the basis for all DCS application.

3.1 WinCC OA Software Environment

After a comprehensive market survey of Supervisory Controls and Data Acquisition (SCADA) systems, WinCC OA from the company ETM[1] was decided on for its high performance and scalability[40]. "OA" stands for Open Architecture, which means that it offers a C++ application programming interface (API) to connect custom software to the system. This can be done with the Data Interchange Protocol (DIP) and Distributed Information Management System (DIM) software components.
WinCC OA can be distributed over a large number of computers and is a data point based and event-driven control system. This means that current information is stored as data point elements in a database, were value changes are handled by an event-based approach using multithreaded callback routines. The option of a distributed system provides scalability. A distributed system means that a WinCC OA project running its processes (called "managers") on one computer can access other projects' data by connecting to them on other computers.

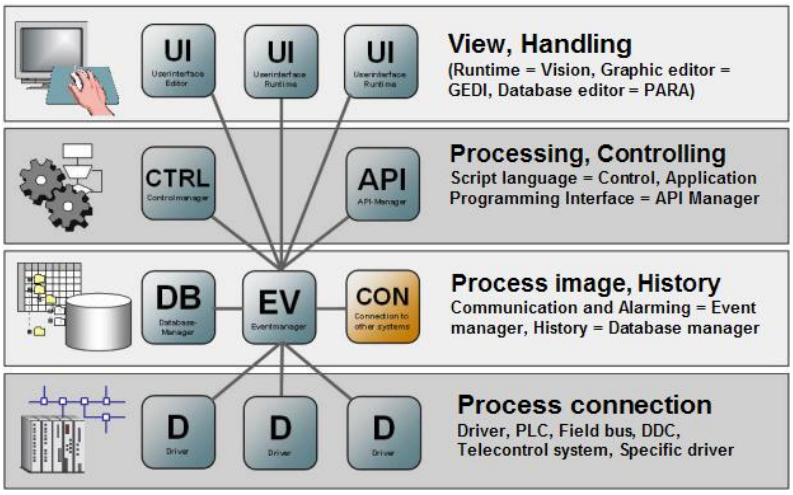

Figure 3.1: Architecture of a WinCC OA system with its managers [43].

The architecture of a WinCC OA project with its managers can be seen in Fig. 3.1. The drivers (D) handle communication with hardware. The Event Manager (EV) is the

[1]SIMATIC WinCC Open Architecture (OA) is a software developed by ETM professional control GmbH, a daughter company of Siemens AG

central processing center in WinCC OA. It always has all current process variables in memory and provides them to other managers as a central data distributor. The EV also performs the alert handling. The Database Manager (DB) is the link to a database where the data points are stored and handles the configuration of data in the database. Queries to historic data are handled by the DB, not the database itself.
The only mandatory managers for a WinCC OA project are the database manager and the event manager, and all other processes can be started when necessary. For the development of scripts and panels, Gedi, an Integrated Development Environment (IDE), is provided. Scripts use a C-like programming language called "Control". Panels can display values of data point elements for control and supervision. Data point elements can be accessed on the user interface provided by the Para program. The Para program shows the data points with its elements grouped in class-like data point types.
The JCOP framework provides a large array of components and libraries useful for the developments of WinCC OA panels and scripts. It provides functionalities, for example components for access control, alarm tools, trending tools, and database configuration. The OPC UA servers provided by the JCOP collaboration are used to connect different power supplies to the WinCC OA system and the software for the Finite State Machine (FSM). A FSM is a formalism specifying the behaviour of an object depending on its state. Detectors like the ATLAS experiment need to automate parts of their operation in order not to overwhelm the operator in the control room. A hierarchical model of the detector parts in the form of a FSM achieves this.

3.2 DCS for the ITk Pixel OB Demonstrator

For the DCS of the ITk Pixel OB demonstrator, both the requirements for ATLAS DCS [40] as well as the DCS requirements for the HL-LHC [44] need to be taken into account. The former are already explained in Chapter 2 and the latter bring an additional focus into the standardization of elements and the integration of detectors within the system.
The demonstrator DCS will have three independent communication paths differing in availability, reliability and granularity [45]:

- Diagnostics: Data from the diagnostics path is delivered from each front end chip, providing information of the highest granularity. The data acquisition system must be running for this path to be available.
- Control and Feedback: The control and feedback path controls the power supplies, SP chains, detector modules and the Opto Boxes. The feedback consists of mainly voltage and temperature information of the modules. It is therefore required during

commissioning, calibration and data-taking periods of the detector and needs to be highly reliable.

- Safety: The safety system requires the highest reliability and runs at all times in the form of the interlock system in order to prevent harm to people and the detector itself.

The architecture of the ITk Pixel Demonstrator DCS with its three paths and their components be seen in Fig. 3.2.

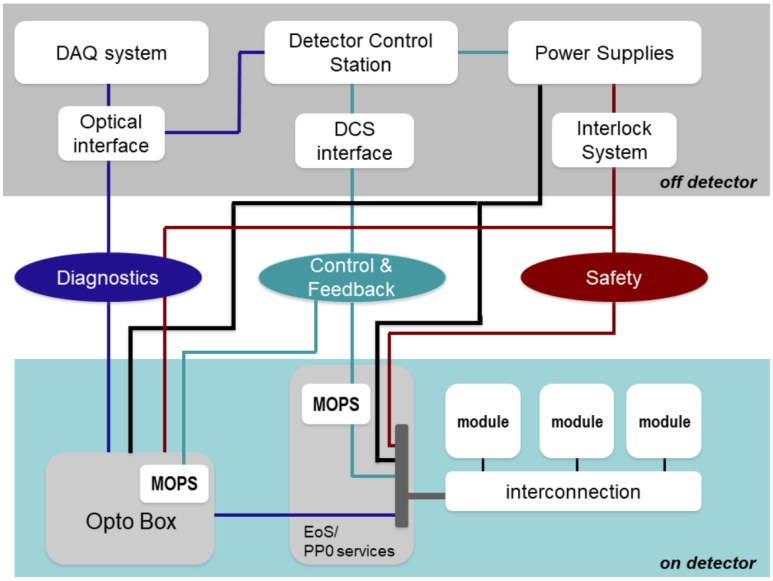

Figure 3.2: Overview on the ITk Pixel DCS with the three different paths of diagnostics, control and feedback, and safety [45].

A dedicated DCS PC is available to run the WinCC OA project, which will be used to control and monitor the demonstrator. WinCC OA 3.16 requires CentOS as a Linux operating system which was chosen due to its long-term technical support.
Some other relevant hardware used in the demonstrator DCS consists of: MOPSHUB4Beginners, interlock/ELMB, SP chains, power supplies and the cooling system. They are explained in turn below.

MOPSHUB4Beginners The MOPSHUB4Beginners is a RaspberryPi which connects via CANbus to several MOPS chips reading their data. The RaspberryPi runs an OPC UA server and connects to the LAN via ethernet. Later on in the development, it is planned to have the WinCC OA project connect with an OPA UA client directly to the OPC UA server of the RaspberryPi of MOPSHUB4Beginners.

Interlock The main component of the interlock is the Interlock Matrix Crate (IMC). The one used in the current demonstrator is already used in the Insertable B-Layer (IBL) detector [46]. The full documentation of the IBL IMC can be found in Ref. [47]. The purpose of the interlock is to protect human beings as well as sensitive detector components. It engages when monitored values cross a predefined threshold. Currently monitored values are temperatures, dew points, box switches and brightness inside the demonstrator box. The input of the IMC is monitored by ELMBs. The ELMBs use Analog Digital Converters (ADC) to convert the incoming voltage into a 12 bits count, which is read out by an CANopen OPC UA server running on a connected PC. On the OPC UA server, the voltage value arriving at the ADC is calculated with the bit count and the reference voltage of the ADC. The IMC currently used in the OB demonstrator setup in SR1 can be seen in Fig. 3.3. Its ELMB cards are labeled with "Monitoring". The input cards have a discriminator which generates a digital signal for the FPGA, the core of the IMC. The FPGA is located in the grey block in the middle of the IMC. It includes the interlock logic and defines how the system should react. This means that after the input crosses the defined threshold, the FPGA sends an interlock signal to the related power supplies.

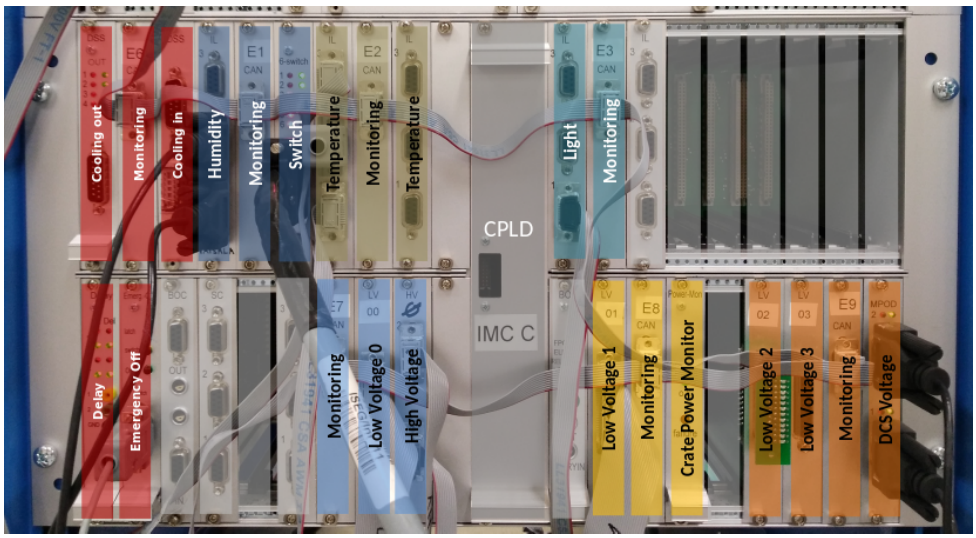

Figure 3.3: Interlock Matrix Crate used in the OB demonstrator in SR1 [46].

Temperature monitoring is done via NTCs (Negative Temperature Coefficient Thermistors). A resistance whose value depends on the temperature is set before the voltage reaches the ADC, so the temperature can be calculated using the monitored voltage value. One NTC is placed on the last module in each SP chain in the direction of the cooling pipe. NTCs are also planned to be placed on the pipes themselves. In the case of temperatures rising over the threshold, the FPGA will receive the discriminator signal from the respective ELMB and turn off the power supplies of the concerned SP chain.

Aside from the temperature, other quantities used as input for the interlock are the dew point, calculated via humidity measurements inside the box, the light intensity inside the box and the box switches. If it is too humid or too bright inside the box or if it is not correctly closed, the interlock shuts off the power supplies of the OB demonstrator.

SP chains The SP chains [33] are the main test object in the OB demonstrator. Each SP chain contains at least 3 and up to 16 modules. Aside from monitoring each SP chain via the MOPS chips, the DCS also needs to control the power of the chain itself with both HV and LV, the optoboard belonging to it and the MOPS chip. The single LV line powering all SP units of a single chain with a constant current source needs to be able to carry a current of up to 8A. Each SP chain must be electrically isolated and all its different power supplies (LV, HV and the power supply for the MOPS chip) need to be referenced to the same ground potential. All modules of a single chain should be monitored by the same MOPS chip. Lastly, every optoboard serves only one SP chain. For safe operation, monitoring should be powered before the modules or the optoboard is switched on, and the LV should power the modules before the FE chips receive their HV.

Power supplies For the low voltage power supply, a current regulated power supply is used, since a constant current is necessary. The high voltage supply is provided by two modules manufactured by *iseg* Spezialelektronik GmbH inside a Wiener Crate. For the control of all power supplies, a second OPC UA server is set up. The Wiener OPC UA server runs on the same PC as the CANopen OPC UA server connected to the interlock system. Both servers automatically start after boot and restart in case of failure.

Cooling system Similar to the IMC, the cooling plant currently used in the OB demonstrator in SR1 is the IBL CO_2 cooling plant [48]. It has a maximal cooling loop flow of 14 g/s and a temperature range from $-35°C$ up to $+20°C$. The operational parameters are published via DIP (Data Interchange Protocol) and transferred into WinCC OA data points with a JCOP component. DIP is a CERN communication system which allows small quantities of real-time data to be exchanged between systems.

4 Panels for Temperature and Voltage Monitoring

The main task of the DCS aside from detector control is the monitoring the detector. In addition to the interlock safety measures, manual monitoring is a useful tool both to predict possible errors before they occur as well as diagnosing them after the fact. The final ITk pixel detector will have a large number of sensors which will need to be monitored. The number of sensors and their types can be seen in Table 4.1. The number of the temperature sensors is very high due to every single module having its own temperature monitoring. Additionally, voltages of the power supply will also be measured for every single module. The OB demonstrator in SR1 will contain only 27 RD53A modules connected in SP chains, but the scalability of the DCS monitoring already needs to be taken into account at this stage. While there are currently sensors for humidity, pressure and the dew point in the box of the OB demonstrator, they are sensors of the environment of the demonstrator, not the demonstrator itself. Sensors for gas flow, radiation, vibration and strain gauges are not yet implemented at this point in the development, since the demonstrator currently consists of a single longeron without mounted modules.

Sensor type	Number of sensors
Temperature	1000
Humidity	30
Pressure	200
Gas flow	20
Radiation	20
Vibration	6
Strain gauges	40

Table 4.1: Numbers of different types of environmental sensors that are planned in the ITk volume. [6]

During the scope of this master's thesis, I created panels for the manual monitoring of single module temperatures and voltages. Focus was placed on the development of panels

showing a single LLS with the temperature and voltage of each module. LLS chains are suitable entities to display in the monitoring since they share a cooling pipe. With two or four SP chains per LLS, all modules of the LLS were fit onto on single panel while still providing readability. Another restriction is the maximum panel size set by the JCOP framework, which would lead to a loss of readability, if more than one LLS is displayed on one panel.
In order to facilitate the monitoring done by real persons, the single module temperature and voltage values will have an associated colour as their background. The spectrum for the temperature values ranges from blue for cold over green to warm for hot. For the voltage values, the optimal value is shown in white and the further away from it the value is, the pinker its field. The two colour spectra can be seen in Fig. 4.1 (a) for the temperature monitoring and (b) for the voltage monitoring. With these spectra, bright red and bright pink are the colours signalling alarming values.

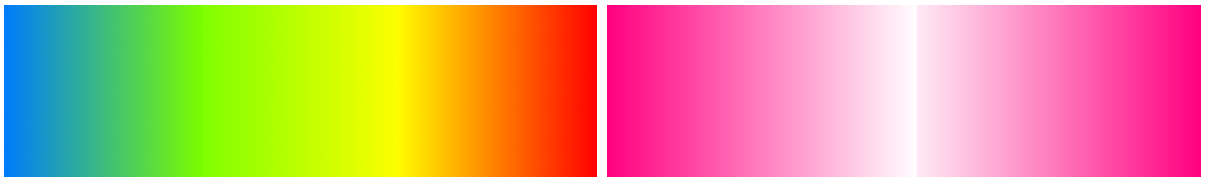

(a) ***(b)***

Figure 4.1: Colour spectra for the monitoring of (a) the temperature values with blue corresponding to the lowest value of the range and red for the highest and (b) the voltage values with white corresponding to the optimal value and pink for the extrema of the range.

Aside from the single module temperature and voltage values, the following information is shown on every panel:

- Identifying information of the LLS chain
- Name of each module
- Which modules are part of the same SP chain
- Placement and direction of the cooling pipe
- Which modules are used as input for the interlock
- What minimum/maximum values the spectra ranges correspond to
- Which modules are front-facing and which are back-facing in the half-rings

The code of the monitoring panels uses only the alias of the depicted LLS as input. The maximum panel size is set by the JCOP framework. All panels depicted in this chapter will display dummy variables for temperature and voltage monitoring.

4.1 Temperature and Voltage Monitoring for Longerons

The first type of LLS of the OB demonstrator are longerons. In the final ITk pixel OB, each longeron will have 4 SP chains, two in the middle next to the interaction point with 6 modules each and two with 12 modules on the outside. Their design can be seen in Fig. 2.10. While the OB demonstrator in SR1 will have only one longeron with one full SP chain, the monitoring panels were given input portraying the full LLS. The panel of the longeron monitoring showing both temperature and voltage values of the modules can be seen in Fig. 4.2.
Due to the maximum panel size, the A-side of the longeron is depicted over the C-side to allow for larger module panels, which are necessary for readability of the monitored values. This means that the interaction point is to the right of the A-side and the left of the C-side. The placement and direction of the cooling pipe is displayed via arrows along the pipe, with a colour coded passage at the interaction point. A legend identifying which longeron in the detector is displayed and how interlock modules are indicated is shown in the left middle of the panel. In the middle to the right are the temperature and voltage values corresponding to the outer ends of the spectra. The modules connected in a single SP chain are contained in a light grey rectangle and the interlock modules are indicated with a black lattice. The identifying information about the longeron displayed is read out via the name of the alias assigned to the data points. Limits representing the extrema of the color spectra are defined in the code. The placement and direction of the cooling pipes is determined by which modules go into the interlock.
The single modules have their name displayed vertically on the left of their box with the monitoring values shown stacked next to it. Names and aliases of the module data point elements are shown as text fields when hovering the mouse over the respective module.
The arbitrarily chosen values for temperature and voltage show that the colour coding helps in identifying which monitored values are problematic.

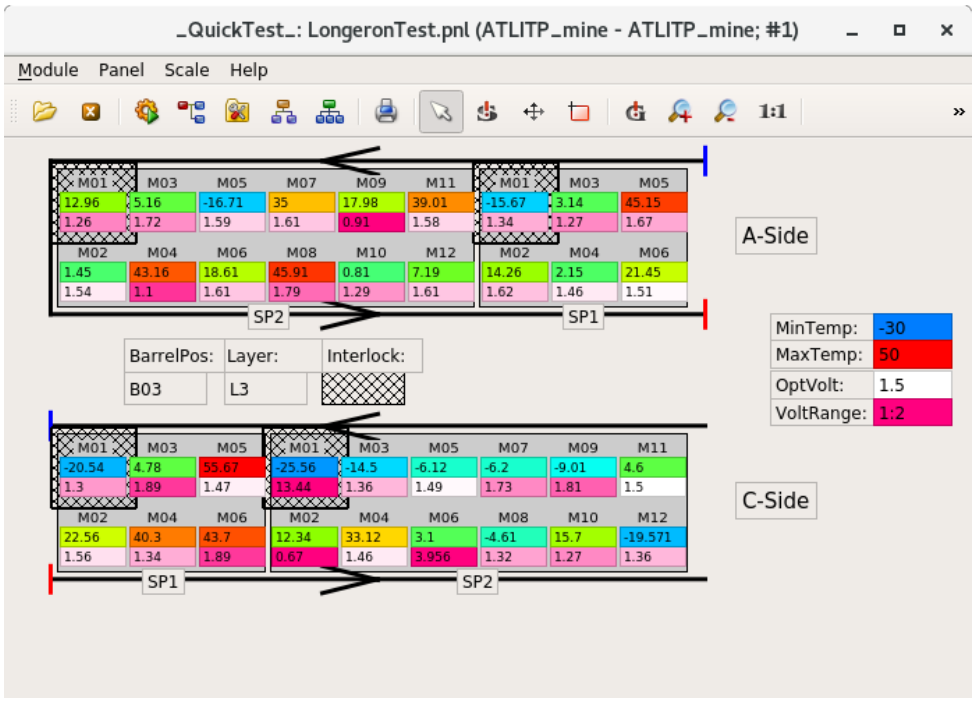

Figure 4.2: Panel for monitoring of longerons displaying temperature and voltage of single modules.

4.2 Temperature and Voltage Monitoring for Half-Rings

Half-rings are the second type of LLS present in the OB of the ITk pixel detector. The inclined half-rings have two SP chains each with 8, 11 or 14 modules per SP chain corresponding to their placement in layer 2, 3 or 4. Additionally, half-rings occur in the top or bottom position of the detector. Their design can be seen in Fig. 2.11. A monitoring panel should make the combination of layer and top/bottom of the current panel clear.
In the OB demonstrator, two half-rings with one full SP chain each are planned, though at present the modules have not yet been installed. Similar to the longerons, the following panels were tested using dummy data points with manually set values. All half-ring monitoring panels contain a legend with identifying information, placement and direction of the cooling pipes, a legend specifying the values corresponding to the extremes of the colour spectra, grey areas indicating the SP chains, and an indication which modules are backwards-facing or are used as input for the interlock.
A panel depicting the layer 3 top half-ring on the A-side can be seen in Fig. 4.3. In contrast to the longerons, the form of the half-rings varies with the three different sizes and the occurrence of both top and bottom half-rings. While the OB demonstrator will

not yet have bottom half-rings, the functionality to display them should already be present in the monitoring. In addition to this, the half-rings are depicted from the point of view of the interaction point of the detector. As a result, it will be clear whether the forwards- or the backwards-facing modules depicted in the panel are closer to the point of interaction. The following half-ring panels are initialized with the alias of the LLS displayed as input. Two SP chains with 11 modules each are mounted on the half-ring of this layer. The placement of the modules on the panel is equivalent to the placement in the final detector.

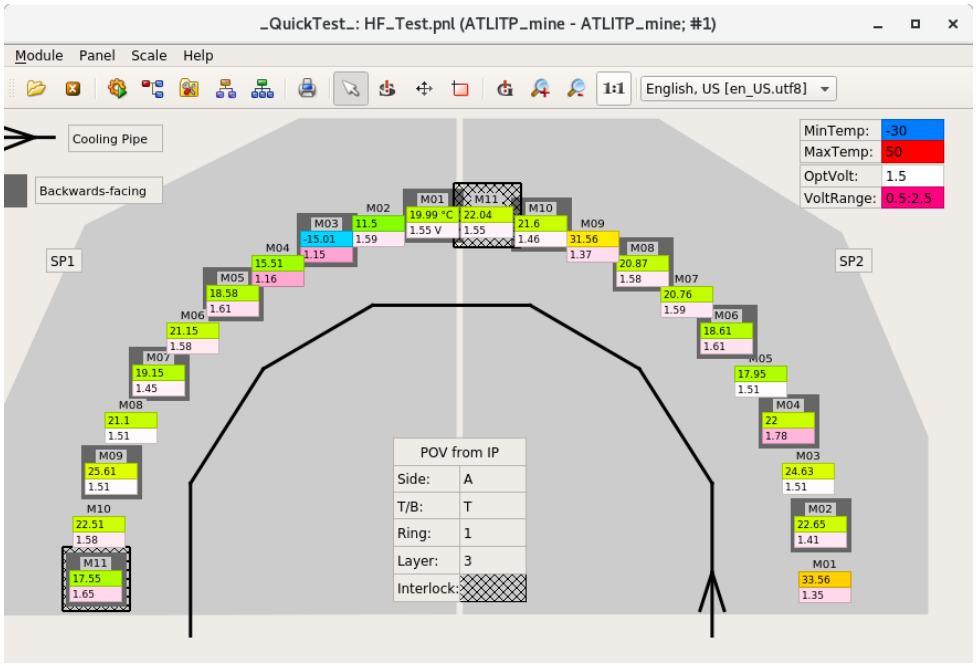

Figure 4.3: Monitoring panel of a top L3 half-ring on the A-side.

The direction of the cooling pipe is counter-clockwise from the interaction point. The information for this comes from the placement of the interlock module as the 11th module in the two SP chains.
A monitoring panel for a layer 4 top half-ring on the A-side can be seen in Fig. 4.4. For this panel, some of the data point elements of the SP chain were missing. The code is robust against this and shows the existing module temperatures and voltages in the correct position and also correctly shows which panels are backwards-facing.

Monitoring panels of half-rings of layer 2 on the C-side can be seen in Fig. 4.5. Fig. 4.5 (a) is a top half-ring and Fig. 4.5 (b) a bottom half-ring. The comparison of the L4 top half-ring on the A-side in Fig. 4.4 and the L2 top half-ring in Fig. 4.5 (a) shows that from the point of interaction, the module numbering is counter-clockwise on the A-side and clockwise on the C-side. This is reflected in the interlock placement and the direction of the cooling pipe.

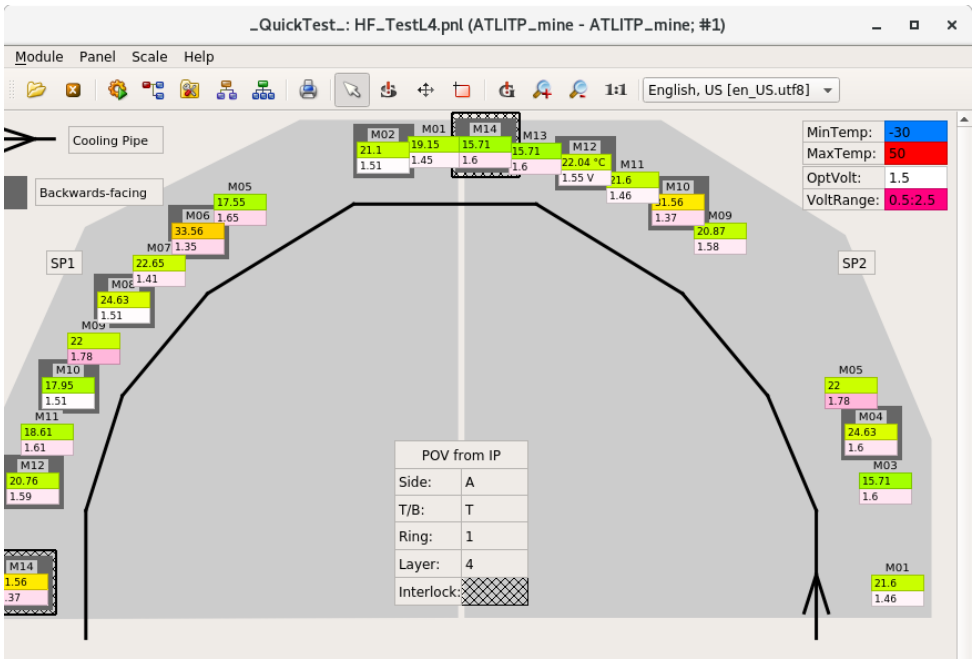

Figure 4.4: Monitoring panel of a top L4 half-ring on the A-side with missing modules.

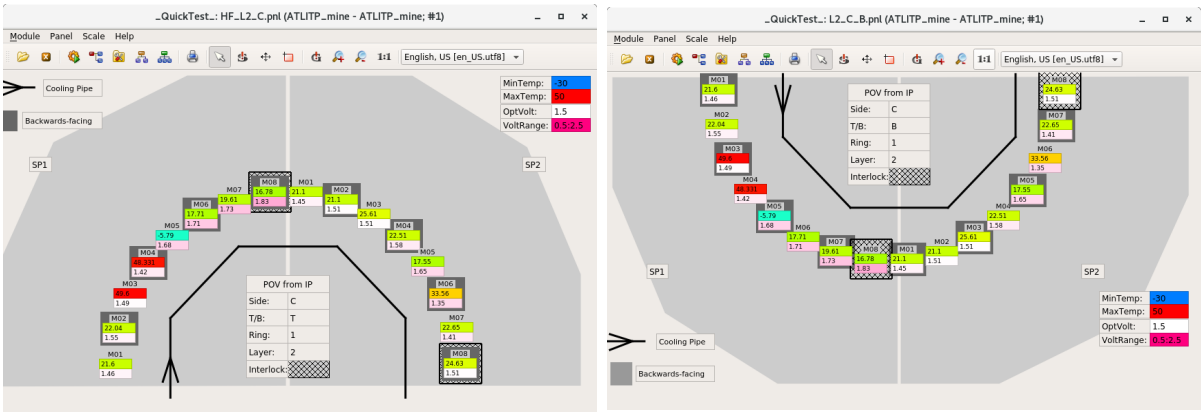

(a) ***(b)***

Figure 4.5: Monitoring panels for a top (a) and a bottom (b) L2 halfring on the C-side.

The monitoring panels of the half-rings depict all necessary information and show clearly which half-ring is depicted based on the module placement. The arrangement of the modules on the panel is in accordance with their future physical layout. Colour coding of the temperature and voltage values helps identify outliers.

4.3 Implementation in the Finite State Machine

The next step in the development of the LLS monitoring panels after testing them locally was to integrate them into the Finite State Machine (FSM) of the OB demonstrator in SR1. The FSM is a tool for monitoring and controlling the OB demonstrator via WinCC OA.

The integrated monitoring panel for a longeron can be seen in Fig. 4.6. Temperature and voltage monitoring values are available, but only in the form of dummy values. The short SP chain mounted on the demonstrator has one interlock module in the form of the M05 module. The cooling pipe placement was correctly determined in the code by the given interlock position. The short SP chain is also placed correctly as the SP1 chain on the A-side of the demonstrator. There are no reasons to expect errors in the module placement once the second SP chain of the longeron and the SP chain on the inclined half-ring are mounted on the demonstrator.

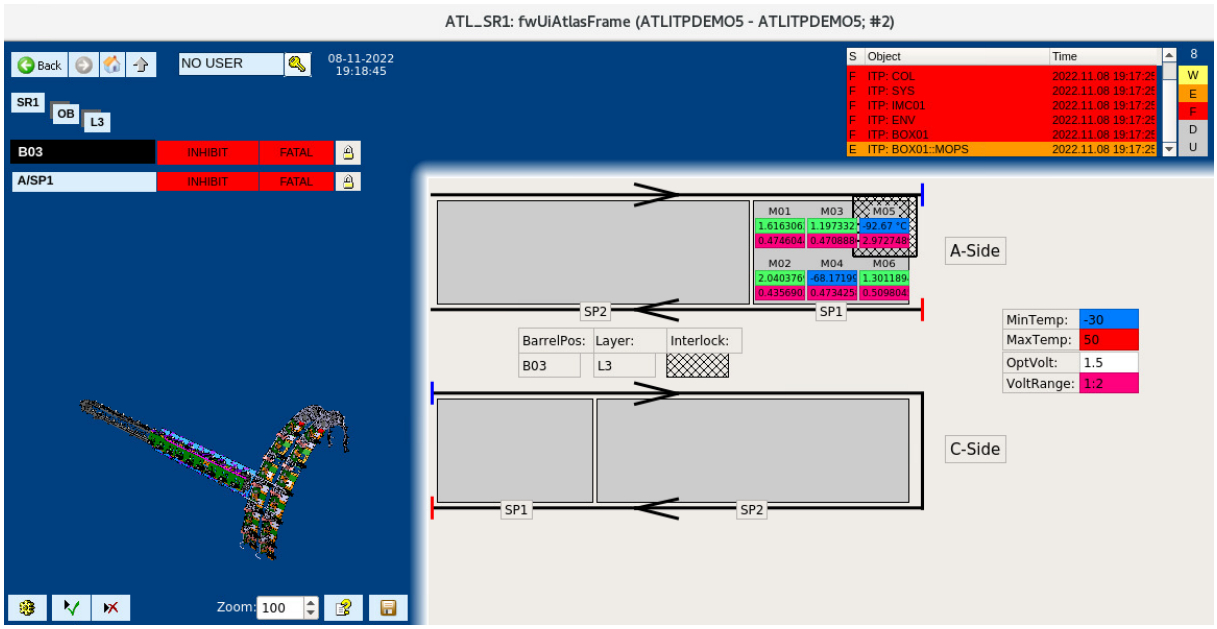

Figure 4.6: Longeron monitoring panel in the OB demonstrator FSM.

The first instance in the development of monitoring panels for LLS in the ITk pixel detector OB demonstrator is now functional. Locally tested, the panels fulfilled their requirements for monitoring, and were successfully integrated into the FSM of the SR1 WinCC OA project. In the future, the monitoring of global values such as humidity, pressure, gas flow etc. can be added to the panels.

5 Archiving

Archiving is an important tool in software monitoring for identifying and solving problems or verifying their absence. WinCC OA provides the functionality of archiving data point elements with the help of dedicated software managers. Without the functionality of an archive, past monitoring data cannot be obtained and therefore can not be used to troubleshoot problems or reconstruct situations. During the scope of my master's thesis I set up archiving for the SR1 OB demonstrator WinCC OA project and created panels facilitating its use.

5.1 NextGen Archiver

For the archiving of data in the WinCC OA project of the SR1 OB demonstrator, the NextGenArchiver (NGA) [49] is used. The NGA is a new WinCC OA archiver developed by CERN and ETM. It is the successor of the RDB Archiver which provides both an InfluxDB and an Oracle backend. InfluxDB, as an open source database, is planned to be used in testing sites outside of CERN. For the SR1 OB demonstrator system test, an Oracle backend will be used.
Archiving many data point elements has a high demand on memory capacity. To mitigate this, while adding an element to the archive a smoothing configuration can be chosen. Only values that fulfill the set criteria are kept in the database. The relevant options for smoothing in the NGA are "Deadband", "Time", "Deadband AND Time", and "Old/New comparison".
Deadband The deadband is defined as the amount that the value of the archived data point element needs to change in order for a new value to be stored in the archive. A new value being stored in the archive is called a value passing the smoothing. Deadband values can be defined as absolute or relative, but in general absolute deabands are recommended. If for example a voltage data point element whose value is 3 V has an deadband smoothing of 0.5 V, a new value for this data point element passes the smoothing as soon as the value becomes lower than 2.5 V or higher than 3.5 V. Deadband values should be chosen in the magnitude of fluctuations relevant for the monitoring of the respective data point

elements.

Time With this smoothing option a time interval is set. As soon as this interval has passed, the next monitored value for the data point element passes the smoothing. In the example of a time smoothing of 1 hour, the currently monitored value of the data point element is archived every hour.

Deadband AND Time This is a combination of the deadband and time smoothing, where a value passes the smoothing if either the defined time has passed or the value changes by more than the defined deadband.

Old/New comparison For the old/new comparison, archived data point elements pass the smoothing as soon as their value changes.

All floating point data point elements added to the database are planned to have "Deadband AND Time" as their smoothing configuration. The deadband value is always set as absolute and the concrete value is geared to the monitored value and its expected fluctuations. All "Time" smoothing will have a tolerance time of 1 hour. Binary values as well as floating point values set manually will be smoothed with "Old/New comparison".

5.2 Archiving Panels in WinCC OA

In the first stage of archiving in the SR1 OB demonstrator, the only way of adding or removing data point elements from the archive was to manually search for a single element in the "params" menu and edit its archiving selection there. However, this is not feasible for the number of archive configurations planned in the project. Therefore solutions were needed to extend the functionality. One option I worked on was bulk configuration, because several data points can be configured at once. The JCOP framework provides panels for archiving configuration which I integrated into the SR1 WinCC OA project.

Any data point elements that have the same smoothing configuration can be added at once to the database in a bulk configuration. The first iteration of a panel opening a bulk archiving configuration can be seen in Fig. 5.1. Data point elements are selected by specifying either their name or alias. The "*" symbol is a placeholder for an arbitrary string. For the data point element name, it is necessary to include all "." characters in the name of the data point element.

If the archiving configuration is opened with the input of the data point element naming convention of "*a2*.Temp" on the panel in Fig. 5.1, another panel which can be seen in Fig. 5.2 is opened. The boxes for "Configure" and "Enable Smoothing" have been ticked in order to open the respective menus. In order to add the selected data point elements to

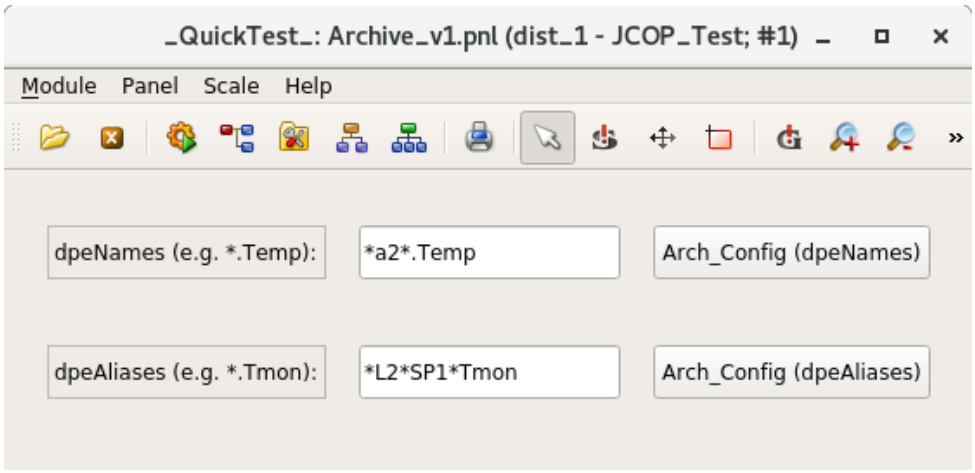

Figure 5.1: Selection panel specifying for which data point elements the archiving configuration panel should be opened, by specifying either name or alias.

the archive, the backend needs to be chosen in "Archive Class" and the "Archiving ON" box needs to be checked. The smoothing configuration can be chosen in the middle of the panel, with time and deadband values set manually if needed. Clicking on "Apply" or "OK" finishes the upload to the database.

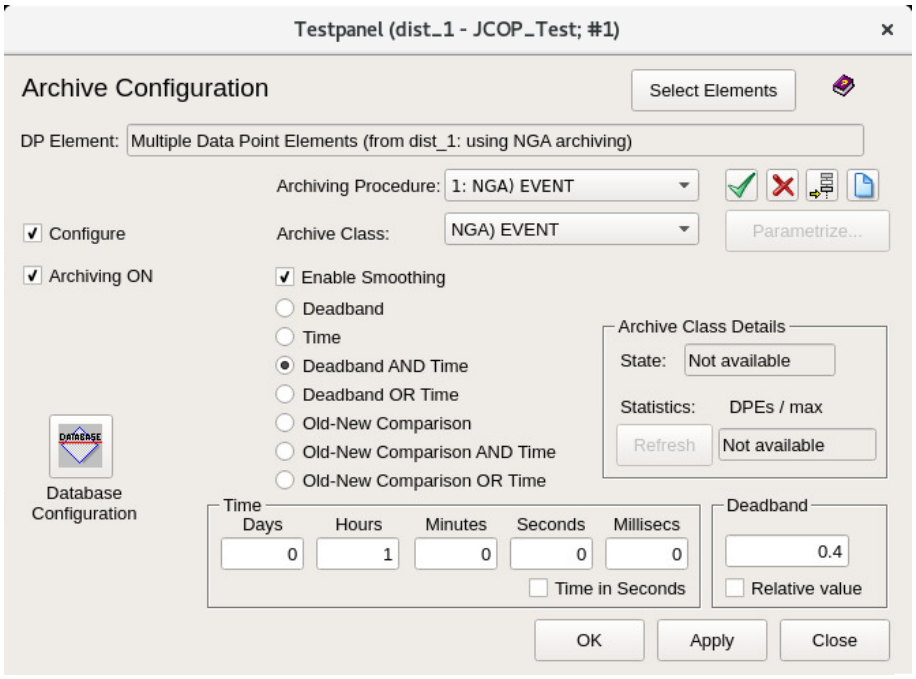

Figure 5.2: Archiving configuration panel opened with the input selection of "*a2*.Temp" as data point element names with a "Deadband AND Time" smoothing setting of 0.4 °C and 1 h.

The data point elements that are selected for the current configuration can be seen if the button “Select Elements” in the upper right corner is chosen. By clicking on “Select Elements”, the panel seen in Fig. 5.3 opens. In this window, the selected data point elements with their name, element type and alias can be seen. With the “Selected” column to the right, a subsequent selection can be made.

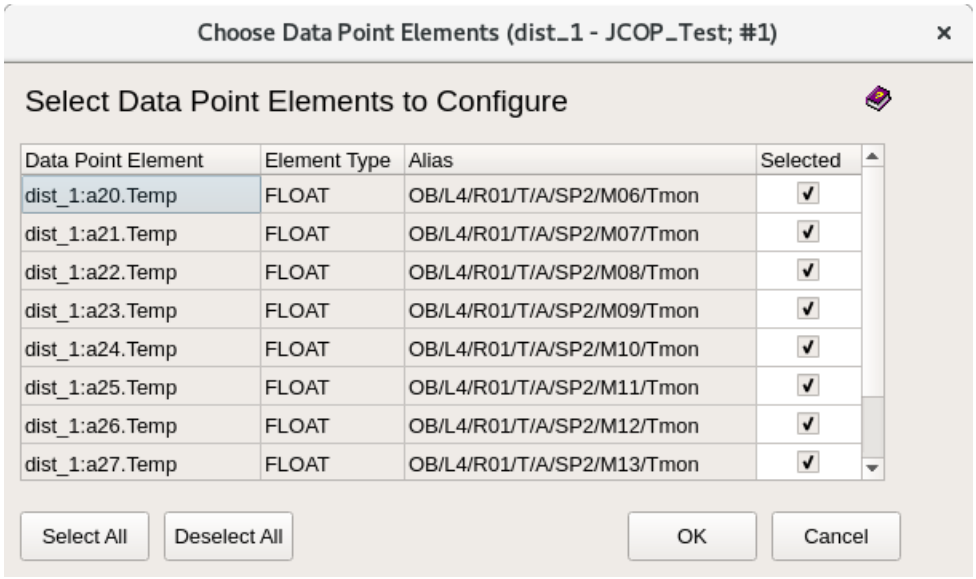

Figure 5.3: Data point elements selected for the current configuration, which were those whose names fit the specification “*a2*.Temp”.

The archiving configuration panel in Fig. 5.2 is a JCOP framework component, the one creating its input in Fig. 5.1 has been created by myself and the panel listing the currently selected data point elements in Fig. 5.3 is a JCOP framework component which I modified by adding the “Alias” column.

5.3 Archived Data Point Elements

A local test of the NGA with an InfluxDB backend was successful in adding data point elements in mass configuration to the database with the respective smoothing. Both adding them by specifying their name or alias worked. The Oracle backend provided by CERN was upgraded from a schema of 8.9 to that of 8.20 in order to be compatible to the NGA. After the upgrade was done, the NGA was installed on all projects in the distributed WinCC OA system.
Once the Oracle database was updated, all relevant data point elements from the OB demonstrator were added to the Oracle database. This list was created with either name

or alias and the respective smoothing configuration. The list contains data point elements from the following four areas, with the number of elements to be added from it in brackets:

- Power supply (242)
- Input interlock (39)
- Output interlock (19)
- Cooling system (51)

This number of data point elements represents a demonstrator with only four full SP chains, where first RD53A modules have been added. The final detector and even later instances of demonstrator system tests will have a multitude of data point elements to be monitored and archived.
The time and deadband limits set for the smoothing of data point elements will need to be evaluated once the database is up and running, with current values of typically 1 h for time and a deadband of one to two orders of magnitude smaller than the data point element. If there is too much data to archive even after the smoothing has been applied, the smoothing can be chosen to be more restrictive. If more information about smoothed data point elements is instead desired, the smoothing should be chosen to be less restrictive.
An example of an archived data point element can be seen in Fig. 5.4. It shows the value of the temperature of the M06 module of the short SP chain of the longeron mounted on the demonstrator over several hours. The smoothing configuration chosen for this data point element is a time and deadband smoothing with 0.5 °C as the deadband and 1 hour as the time value. For the first few hours, the graph shows one value per hour, as due to the temperature being relatively stable, the monitored value only passes the time smoothing. At 14:20, the temperature rises due to the SP chain being turned on and the deadband of 0.5 °C is exceeded frequently until at 16:00, when the SP chain is turned off again. As soon as the value changes, new values of the data point element are stored very frequently in the archive, whereas the the monitored value is stored once per hour when nothing of note is happening. The chosen deadband might be considered too small if the temperature fluctuations of the powered SP chain are seen as negligible.

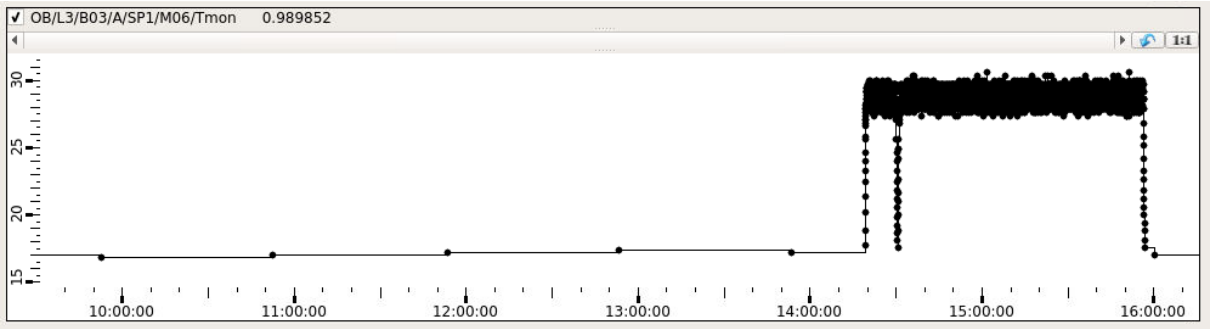

Figure 5.4: Multitrend panel showing the temperature value of the M06 module of the short longeron SP chain in the OB demonstrator over several hours.

6 Voltage and Temperature Calibrations for MOPS and Interlock Chips

During the scope of my master's thesis I implemented three improvements to the temperature and voltage monitoring of the OB demonstrator DCS. The first is the use of a new conversion formula which calculates the temperature based on the resistance of the NTC. The parameters for this new formula are utilized in the temperature-dependence function of the NTC as provided by the manufacturer. I validated the data provided by the manufacturer in climate chamber measurements of three NTCs. The second improvement is the implementation of the ADC calibration of the MOPS chip used in the monitoring of the short SP chain of the longeron. Thirdly, I implemented an absolute calibration of the temperature monitoring of the optobox MOPS chip encompassing both the NTC conversion and the ADC calibration, since an independent ADC calibration was not possible for this chip. This absolute calibration was done with climate chamber measurements.
MOPS chips are an ASIC used in the control and feedback path of the ITk pixel DCS. They monitor the voltage and temperature of the detector modules independently from the data acquisition, with one chip being used to supply values of multiple modules in a SP chain. The temperatures are measured via NTC and the incoming voltage is converted by an ADC. MOPS monitoring is in place for the modules mounted on the SP chains and for the optobox in the demonstrator setup. The module of each SP chain that is used as input for the interlock is not read out by the MOPS system, since its temperature is used as input for the interlock system. Its temperature and voltage are monitored via an ELMB, with the same type of NTC but a different type of ADC. The mode of operation for both MOPS and interlock monitoring of voltage and temperature can be seen in Fig. 6.1.

In the case of voltage measurements, U_{in} is variable while R_1 and R_2 are fixed. R_1 is the resistance used to decrease the incoming voltage into the range measurable by the ADC and R_2 is used for grounding in order not to damage the ADC. Measuring U_{ADC},

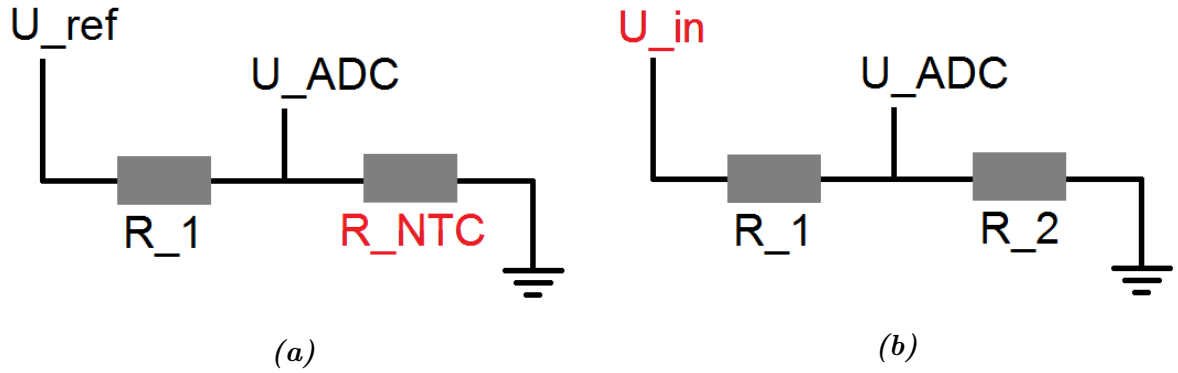

(a) *(b)*

Figure 6.1: Schematic diagram for ADC measurements for (a) temperature and (b) voltage with the respectively monitored value in red.

U_{in} can be calculated:

$$U_{in} = \frac{R_1 + R_2}{R_2} \cdot U_{ADC} \tag{6.1}$$

For temperature measurements, U_{ref} and R_1 are fixed while R_{NTC} is variable and can be calculated by measuring U_{ADC}:

$$R_{NTC} = \frac{U_{ADC}}{U_{ref} - U_{ADC}} \cdot R_1 \tag{6.2}$$

The temperature was then calculated with the resulting R_{NTC} with a formula provided by the NTC manufacturer.

6.1 Improved NTC Temperature Conversion

The temperature of the optobox and the modules in the OB demonstrator was previously calculated from the NTC resistance R_{NTC} measured via the monitoring with the equation

$$\frac{1}{T} = \frac{1}{T_0} + \frac{1}{B} \ln \frac{R}{R_0}, \tag{6.3}$$

fit around $T_0 = 25°C$ with B and R_0 taken from the data sheet provided by the manufacturer [50]. The NTC types used for the temperature monitoring of the modules in SR1 are NTCG163JF103FT1S for the interlock NTCs in the optobox and NTCG103JF103FTDS for the NTC on the modules [51], both of which are manufactured by the TDK Corporation. Though they have slightly different operating temperature ranges with the interlock NTC NTCG163JF103FT1S being –40°C to +125°C, and the module NTC

NTCG103JF103FTDS ranging from –40 to 150°C, the R-T dependence of both is the same. The parameters provided by the manufacturer of $R_0 = 10\ \mathrm{k\Omega}$ and $B = 3435°\mathrm{C}^{-1}$ for $T_0 = 25°\mathrm{C}$ are used for both. Both NTCs have a systematic error of $\pm 1\%$ on R_0 and B. Eq. 6.3 is a simplified version of the Steinhart-Hart equation

$$\frac{1}{T} = (A + B \cdot \ln(R) + C \cdot (\ln(R))^3), \tag{6.4}$$

with T in Kelvin and R in Ohm, which is commonly used for the conversion of NTC resistance into temperature. By using three parameters instead of two as in Eq. 6.3, the Steinhart-Hart equation can provide a more exact fit and therefore improves the accuracy of the temperature monitoring. Additionally, the fit should not center around $T_0 = 25°\mathrm{C}$, but instead be fit in the temperature interval relevant for the demonstrator setup.
The temperature range relevant for the module monitoring in the technical requirements and specifications for the ATLAS ITk Pixel Services is -45°C to + 60°C [33], and in the Technical Design Report for the ATLAS Inner Tracker Pixel Detector, it is -40°C to + 40°C [6]. As a compromise between these two ranges and with regards to the demonstrator setup in SR1, the range of -40°C to + 50°C was chosen as the fit interval.
The temperature dependence of the NTCG103JF103FTDS and NTCG163JF103FT1S NTCs can be seen in Fig. 6.2 in blue, with the previous fit provided by the manufacturer in green and the fit with the Steinhart-Hart equation in the relevant interval in red. It can already be seen that the new fit is a significant improvement. Especially in the high resistance and low temperature range, the previous fit exhibits large discrepancies to the correct values. Even though the old fit is within the upper boundary of the relative error of the data provided by the manufacturer, it has a clear systematic discrepancy with the correct value.

In order to better demonstrate the improvement of the accuracy of the temperature conversion, I calculated the respective temperature differences to the correct temperature for both the new and the old fit in the relevant temperature interval. This can be seen in Fig. 6.3. As expected, the difference of the old fit to the data is 0 at +25°C and becomes worse the farther away from this nominal temperature, with the difference reaching over 4°C at -40°C. The new fit shows a difference under 0.1°C to the data for all values in the relevant temperature interval and is therefore a clear improvement.

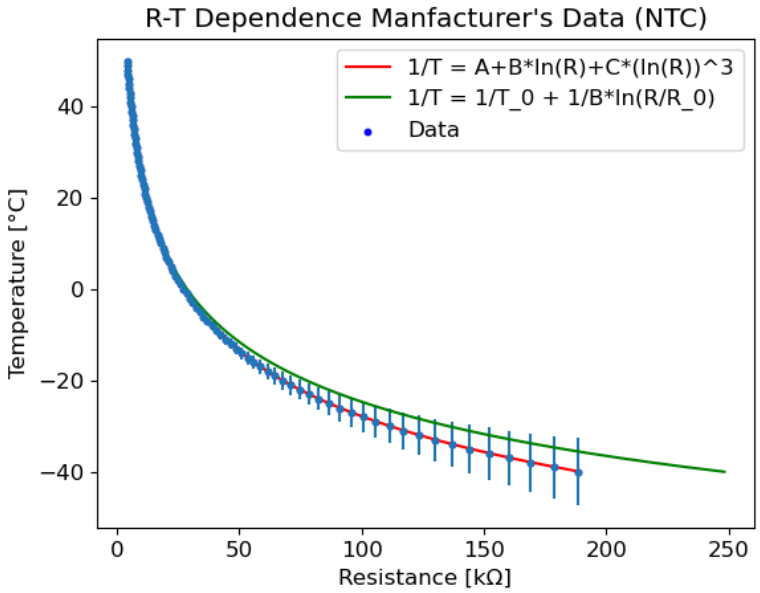

Figure 6.2: Resistance vs. temperature for NTC from manufacturer's data (blue) previous fit (green) and new fit (red).

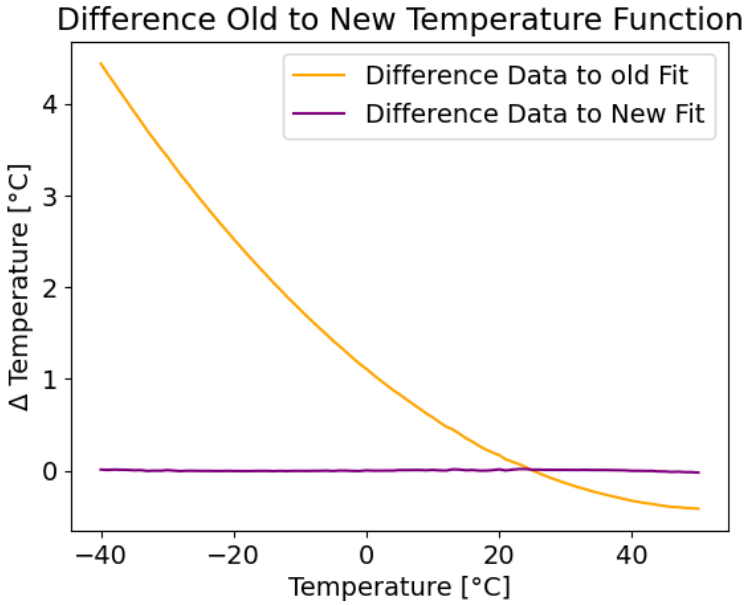

Figure 6.3: Temperature vs. temperature differences for previous (yellow) fit of Eq. 6.3 and the new fit of the Steinhart-Hart Eq. 6.4 (purple) to the manufacturer's data

The parameters for the fit of the Steinhart-Hart Eq. 6.4 used in Fig. 6.2 and Fig. 6.3 are

$$\begin{aligned} A &= (8.95049 \pm 0.00907) \cdot 10^{-4} && [\frac{1}{\mathrm{K}}] \\ B &= (2.50348 \pm 0.00150) \cdot 10^{-4} && [\frac{\ln(\Omega)}{\mathrm{K}}] \\ C &= (1.96051 \pm 0.00603) \cdot 10^{-7} && [\frac{(\ln(\Omega))^3)}{\mathrm{K}}] \end{aligned} \tag{6.5}$$

The errors arise from both the error on the resistance provided by the manufacturer and the fit itself.

6.2 ADC Calibration of MOPS Chips

There are two MOPS chips currently in use in the OB demonstrator setup. One is used for the monitoring of the short SP chain in the longeron and the second for the monitoring of the optobox. For the MOPS chip used in the short chain, there are measurements of the incoming voltage vs. the expected and the measured counts. The counts are the result of the digital conversion of the incoming voltage via the ADC and they are sent from the ADC to the OPC UA server. For the optobox chip, these measurements are not available. It is also not possible to perform the necessary measurements for this chip without deconstructing the optobox. Therefore an absolute calibration for the optobox, which will be presented in Chap. 6.3.2, was performed.
The ADC calibration of the MOPS chip used in the monitoring of the short SP chain of the longeron is based on measurements performed by the group in the University of Geneva, where an independent voltage source was applied to the ADC and the resulting counts were measured [52].
The conversion of the voltage coming into the ADC into the bit count sent to the OPC UA server uses the formula

$$N_{Count} = \frac{4096}{U_{ref}} \cdot U_{ADC}. \tag{6.6}$$

U_{ref} is the reference voltage representing the maximum voltage that can be converted by the ADC and $U_{ref} = 1.25$ V for the MOPS chips used in the OB demonstrator for the monitoring of the SP chains, which is MOPS chip 10. The resistance R_1 in Fig. 6.1 (b) is used to ensure that U_{ADC} does not exceed this value. 4096 is the maximum number possible to represent as a 12-bit integer and is therefore the maximum count measurable by the ADC.
The count measured via the ADC was found to be different from the expected count for several MOPS chips. Generally, the ADC count is expected to be proportional to voltage measured, as can be seen in Eq. 6.6 with the proportionality factor defined by the reference voltage of the ADC and the maximum count. This is not the case for MOPS chip 10. The measurements for MOPS chip 10 can be seen in Fig. 6.4. Chip 10 is in use in the OB demonstrator as the MOPS chip monitoring the short SP chain on the longeron. Since its functionality is used to monitor and evaluate the current detector setup, a calibration was

necessary. Future MOPS chips used in the demonstrator will be measured beforehand to see whether calibrations are needed.

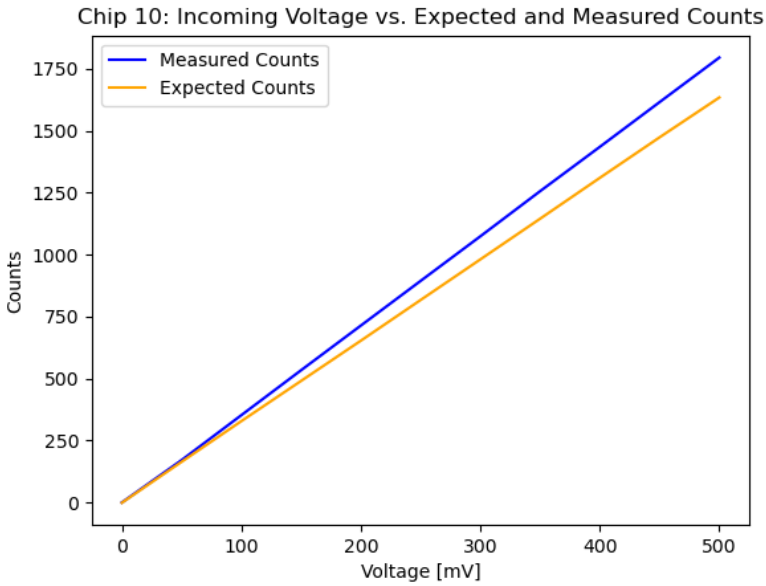

Figure 6.4: Incoming voltage vs. measured (blue) and expected counts (orange) for the MOPS chip 10.

Since the difference between the measured and expected counts is approximately linear, a linear function was fit to it with two parameters. The value the calibration uses is the measured count N_{Count}, so the linear function is of the form

$$N_{Counts,corr} = N_{Count} \cdot (1 - m) - b. \tag{6.7}$$

The fit to the difference N_{Diff} between measured and expected counts in dependence of the measured counts N_{Counts} expressed as

$$N_{Diff} = m \cdot N_{Counts} + b. \tag{6.8}$$

The fit of the linear function to the difference between measured and expected counts with these parameters can be seen in Fig. 6.5. The parameters for this fit are

$$\begin{aligned} m &= 9.148 \pm 0.145 \\ b &= -4.982 \pm 1.534 \end{aligned} \tag{6.9}$$

It shows the measured counts vs. the difference between measured and expected counts from the provided data as well as the linear fit applied to this difference. It is clear that

the linear fit is a good choice for modelling the difference. Except for a short interval at the lowest counts, the two curves are very close.

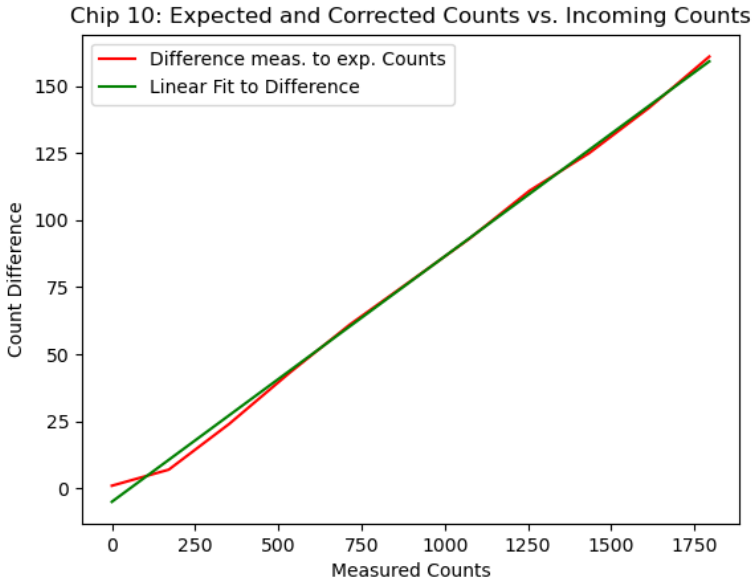

Figure 6.5: Measured counts vs. the difference between measured and expected counts (red) and the linear fit to this difference (green).

Measurements for the incoming voltage vs. the expected and measured counts will be provided for all new MOPS chips used in the OB demonstrator and later on in the detector. As a result, the ADC calibration for further MOPS chips can easily be incorporated.

6.3 Climate Chamber Measurements

The aim of the climate chamber measurements was to measure the resistance of different NTC thermistors at set temperatures, either as direct resistance measurements for the interlock and module NTC or indirectly via the MOPS monitoring for the optobox NTC. With the resulting measurements, it is possible to implement the absolute temperature calibration of the optobox MOPS NTC and validate the new NTC temperature conversion formula for the interlock and module NTC.
The indirect measurements of the optobox channels are done via the MOPS readout. From the temperature recorded for the optobox MOPS channels, values for the resistance can be recalculated. Afterwards, a fit in the form of the Steinhart-Hart equation from Eq. 6.4 is applied, which includes the error arising from the uncalibrated ADC in the MOPS chip. This error is due to the fact that Eq. 6.6 does not correctly describing the behaviour of

the ADC. The direct measurements of a module NTC as well as the interlock connector board and power board in the optobox are measured with a multimeter.

6.3.1 Climate Chamber Experimental Setup

The experimental setup of the climate chamber measurements can be seen in Fig. 6.6. Fig. 6.6 (a) shows the complete setup in SR1 with the PC used to read out the multimeter on the left, the multimeter in the middle and the Arduino thermometer above the climate chamber with a hose injecting dry air into the chamber. Fig. 6.6 (b) shows the inner part of the climate chamber with the optobox in the upper part, with the grey cable connecting the optobox NTC to the MOPS and the blue cables connecting the two optobox interlock NTCs to the the Keithley 2000 multimeter [53]. In the lower part of the climate chamber, the single module NTC is connected to the multimeter.

(a) ***(b)***

Figure 6.6: Experimental setup of the climate chamber measurements of the optobox, module and interlock NTC in SR1 (a) with a closer look inside the climate chamber (b).

The sensors used in the measurements are listed in Table 6.1. The temperature of the climate chamber can be read out on its display. In addition to this, the Arduino thermometer was used as a second temperature sensor, in case the climate chamber sensor was uncalibrated. The third temperature sensor, in form of a Chauvin thermometer, was introduced after the measurements took place, since the temperature measurements between the first two sensors differed by over 0.5 °C. The Chauvin thermometer validated the Arduino thermometer, whose temperature values will be used for the fits. The Arduino thermometer also contained a humidity sensor displaying the current dew point.

Sensor	Readout System
Climate chamber temperature	Climate chamber
Envorinmental NTC	Arduino (MOTH-board) thermometer
J-thermocouple	Chauvin thermometer (abs. calibration)
Optobox MOPS NTC	MOPShub
Optobox Interlock NTC	Multimeter
Single Module NTC	Multimeter

Table 6.1: Sensors with their respective readout system used in the climate chamber measurements.

Before the measurements could start, an experimental procedure had to be determined. For this it was necessary to set an appropriate equilibrium time as well as temperature steps. During all experimental steps the Arduino sensor was checked such that the dew point inside the climate chamber was below the current temperature in order to ensure the safety of the electronics.
Equilibrium time is the time necessary for the inside of the climate chamber to reach thermal equilibrium. The equilibrium time between measurements was determined with test measurements. The last value to reach thermal equilibrium inside the chamber was the interlock power board NTC inside the optobox. After the climate chamber was set to cool down to a temperature of 0 °C, its resistance was measured over a time period of 1 hour. This measurement can be seen in Fig. 6.7. For a measurement period of 10 min after an equilibrium time of 1 hour, the the temperature drift was found to be equal to approximately 0.02 °C. This was deemed as small enough to be negligible.

The temperature ranges of the measurements were chosen due to sensitive components, namely the bPOL12V converter in the module [54] and the GBCR, a gigabit transceiver used in the optobox [55], which is part of the readout chain at PP1. The maximum temperature for measurements was chosen to be +30 °C due to the recommended operation conditions of the bPOL12V converter. The minimum temperature was chosen as -10 °C due to the recommended operation conditions given for the GBCR. Temperature steps of 5 °C were chosen due to the overall time constraints of the measurements.
In the final experimental procedure, the temperatures between +30 °C and -10 °C were measured in steps of 5 °C. When a new temperature was set in the climate chamber, measurements were taken in a 10 min interval after the equilibrium time. The value was then averaged over the measurements in this interval. Before a new temperature was set in the chamber, the dew point of the Arduino sensor was checked in order not to damage the electronics. The measurements at -5 °C, 0 °C and +5 °C were performed

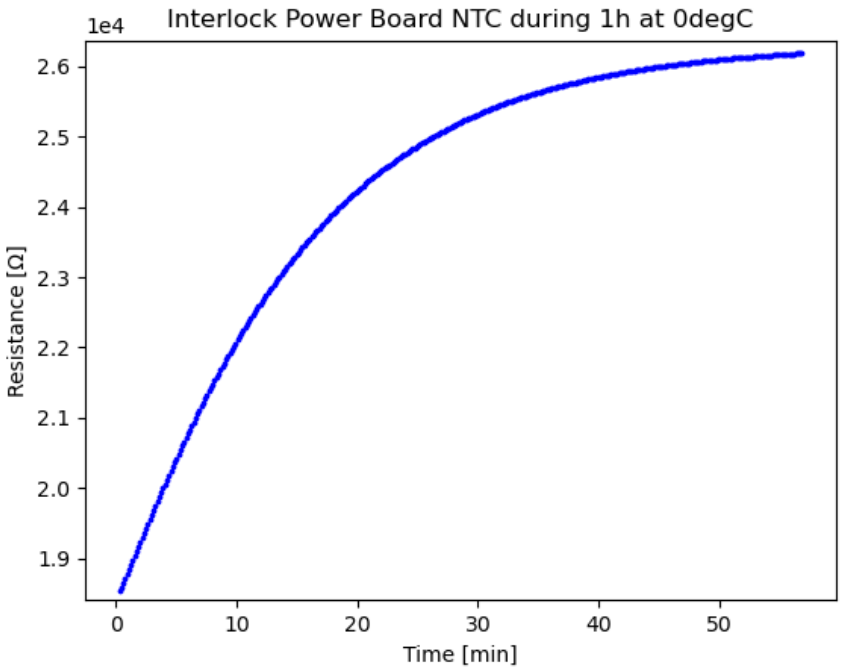

Figure 6.7: Time vs. resistance for interlock power board NTC inside optobox.

twice, once during the cooling down phase and once during the warming up phase to the set temperature. No difference was found in the resulting measured values.

6.3.2 Absolute Calibration of Optobox MOPS Chips

The Arduino thermometer was used for measuring the temperature during the climate chamber measurements. It differed by about 0.7 to 0.8 °C to the climate chamber sensor. The optobox MOPS has eight optochannels monitoring the temperature, whose output was recorded in °C and then recalculated into the resistance value it was based on. The results of the measurement can be seen in Table 6.2. The temperature of each measurement step is given by the Arduino thermometer, with the statistical error on the temperature arising from averaging over the 10 measurement period. The measurement of the optochannels was taken in units of °C, with the error arising from averaging over all optochannels. The formula used to recalculate the resistance based on the temperature monitored by the optochannel, obtained by rearranging Eq. 6.3, is

$$R = R_0 \cdot \exp(B \cdot (\frac{1}{T} - \frac{1}{T_0})), \tag{6.10}$$

with R in Ω and T in K. With this formula, the resistance of the optochannel measurements in Table 6.2 was calculated. The errors on the Arduino sensor are statistical. The error on the optochannel value is the standard deviation of the single channels to the average, with the statistical errors were too small to be taken into account. Systematic errors on the Arduino thermometer or single optochannels were also not taken into account.

Temp. Arduino [°C]	Temp. Optochannels [°C]	Res. Optochannels [Ω]
30.78±0.03	32.29±0.12	7595± 67
25.87±0.03	27.60±0.11	9051± 75
20.85±0.03	22.95±0.12	10832± 99
15.88±0.04	18.28±0.10	13040± 100
10.81±0.04	13.68±0.10	15760± 130
5.82± 0.05 (cool)	9.16± 0.09	19090± 160
5.85± 0.03 (warm)	9.19± 0.09	190650± 150
0.78± 0.03 (cool)	4.73± 0.10	23170± 200
0.74± 0.03 (warm)	4.65± 0.11	23260± 230
-4.27±0.04 (cool)	0.45± 0.08	28122± 210
-4.27±0.04 (warm)	0.43± 0.09	28140± 220
-9.26±0.03	-3.71±0.10	34140± 320

Table 6.2: Measurement results for the optobox MOPS channels.

The measurement steps marked with "(cool)" were taken during the cooling down phase of the climate chamber and the steps marked with "(warm)" during the warming up phase. It can be seen that for both steps the data is within the error ranges, which is a good indicator that the equilibrium time was long enough and thermal equilibrium was reached for each measurement. The fit for the absolute calibration of the optobox MOPS chip to the Steinhart-Hart Eq. 6.4 will use the average between the respective "(cool)" and "(warm)" measurement steps.

A plot of the data of the MOPS optochannels can be seen in Fig. 6.8. The error on the resistance of the optochannels is small enough to be nearly indistinguishable from the data points. The Steinhart-Hart equation is a good fit for the data points in our measurement interval. The previous fit of Eq. 6.3 with $R_0 = 10\ \mathrm{k}\Omega$ and $B = 3435°\mathrm{C}^{-1}$ for $T_0 = 25\ °\mathrm{C}$ shows the best agreement with the data at +30 °C. The lower the temperature, the larger the discrepancy with the data becomes. At −10 °C, the discrepancy between the old fit and the data is over 50 kΩ.

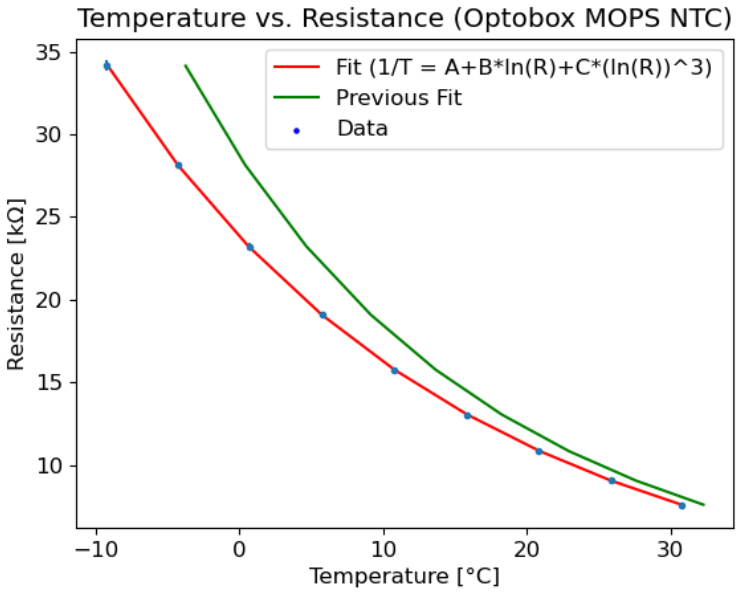

Figure 6.8: Temperature vs. resistance for climate chamber measurements (blue), Steinhart-Hart fit (red) and previous fit of Eq. 6.3 (green).

The parameters A, B and C from this fit, which will be used in Eq. 6.4, are

$$\begin{aligned} A &= (1.45529 \pm 0.07420) \cdot 10^{-3} && [\frac{1}{\mathrm{K}}] \\ B &= (1.55873 \pm 0.11730) \cdot 10^{-4} && [\frac{\ln(\Omega)}{\mathrm{K}}] \\ C &= (6.20054 \pm 0.43222) \cdot 10^{-7} && [\frac{(\ln(\Omega))^3)}{\mathrm{K}}]. \end{aligned} \tag{6.11}$$

The temperature difference at different temperatures for the old conversion and the conversion based on the new fit of the absolute calibration of the optobox MOPS channels can be seen in Fig. 6.9. It is clear that the new fit leads to a more exact temperature monitoring than the old one. While more statistics would have benefited the fit, the results are sufficient for the current OB demonstrator setup. In contrast to the fit of the manufacturer's data in Fig. 6.3, the previous fit of Eq. 6.3 with $R_0 = 10$ kΩ and $B = 3435°\mathrm{C}^{-1}$ for $T_0 = 25$ °C does not yield the correct temperature at $T = 25$ °C. The reason for that is the uncalibrated ADC conversion of the chip used in the optobox. Comparing Fig. 6.9 and Fig. 6.3, it is evident that at lower temperatures, the temperature difference for the old fit is larger. The new fit is currently used for the NTC conversion of the measured NTC in the OB demonstrator temperature monitoring.

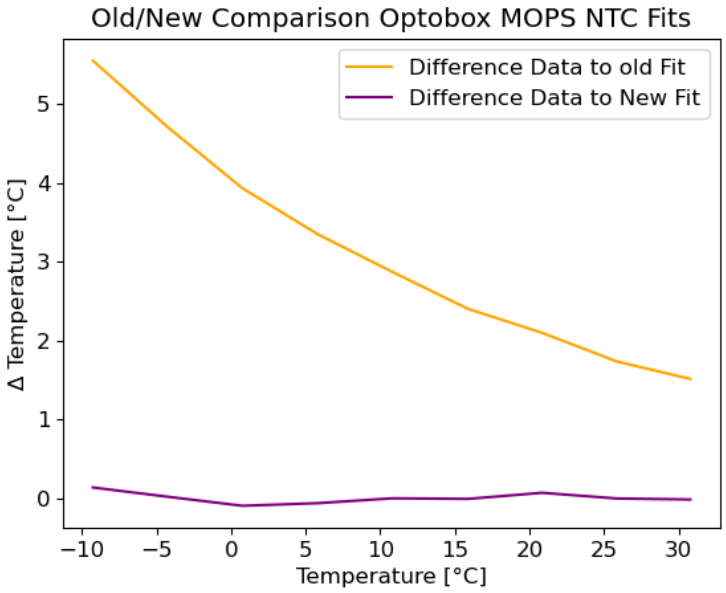

Figure 6.9: Temperature vs. temperature difference for previous NTC conversion with Eq. 6.3 (orange) and new NTC conversion with the Steinhart-Hart Eq. 6.4 (purple).

6.3.3 Validation of Manufacturer's Data for Module and Interlock NTCs

The results of the single NTC climate chamber resistance measurements next to the manufacturer's data can be seen in Fig. 6.10 for (a) the interlock connector board, (b) the interlock power board, and (c) the single module NTC. The climate chamber data is shown in blue, the manufacturer's data is shown in green, the fit applied solely on the climate chamber data is shown in red and the fit based on the manufacturer's data is shown in yellow. For the two interlock NTCs in Fig. 6.10 (a) and (b), the temperature-dependence of the resistance seems to be the same for the manufacturer's data and the climate chamber data. The fits of both types of data to the Steinhart-Hart equation in red and yellow are close to identical in the temperature range of the climate chamber data. For the single module NTC in Fig. 6.10 (c), the manufacturer's data differs slightly with the climate chamber data, which can be seen in the fit on the climate chamber data in red having a slightly higher resistance at -10 °C than the fit on the manufacturer's data in yellow.

In order to better gauge what the difference is between choosing the manufacturer's data and the climate chamber measurements as the basis for the Steinhart-Hart equation fit, we can consult the temperature differences between them at set temperatures in Fig. 6.11. Both the interlock connector and power board NTC have a difference of below 0.3 °C

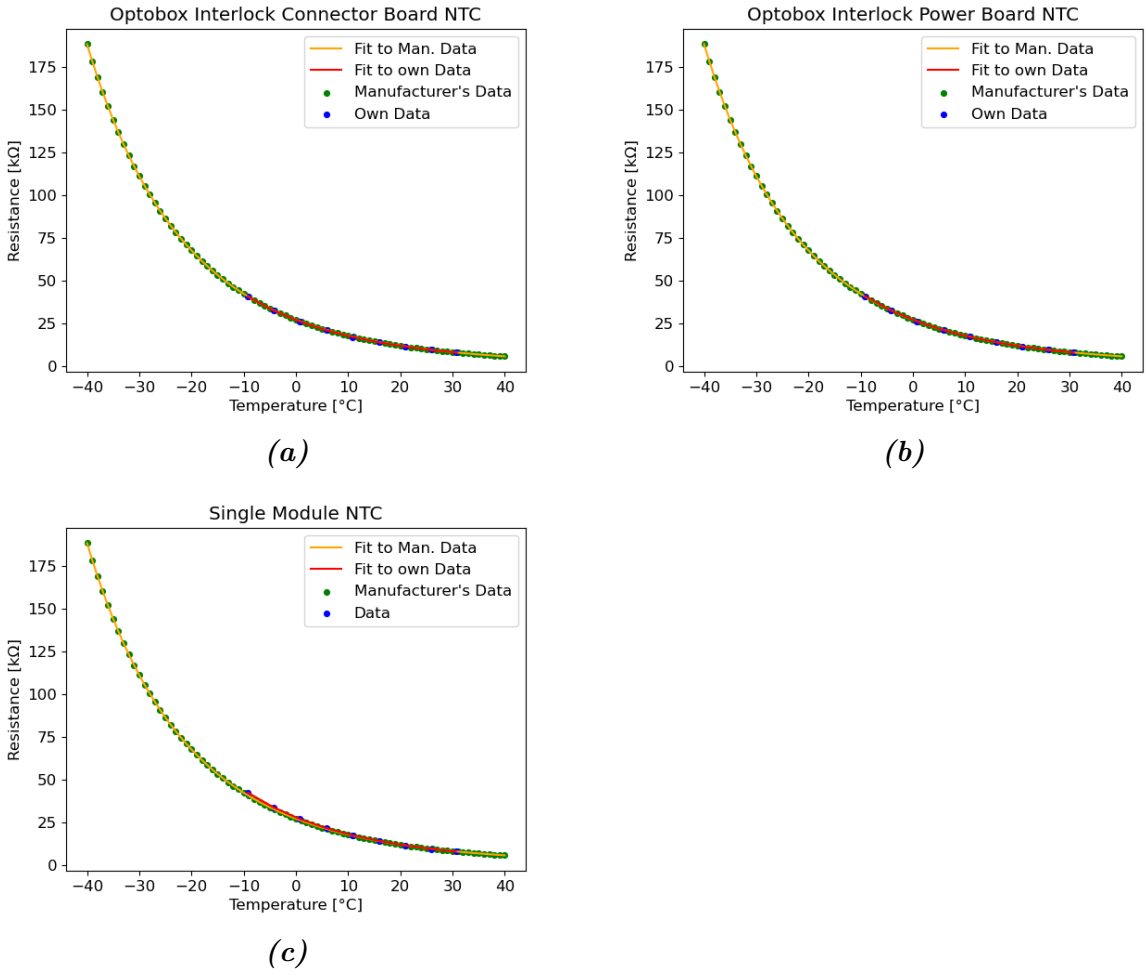

Figure 6.10: Temperature vs. resistance from climate chamber measurements and manufacturer's data for optobox interlock connector board (a), power board (b), and the single module NTC (c) with respective fit in Steinhart-Hart equation.

to the fit on the manufacturer's data in the temperature interval measured in the climate chamber. The single module NTC has a larger discrepancy, with over 0.8 °C difference at -10 °C.

The resistance values of the single NTC climate chamber measurements can be seen in Table 6.3. The statistical errors for the temperatures and resistances arise from averaging over the 10 min measurement period. The systematic errors for the resistances arise from the accuracy of the Keithley multimeter [53], which is 0.01% of the measured value plus 0.001% of the measured range of 100 000 kΩ.
The discrepancy between the two interlock NTC lies within the 2σ interval for the highest two temperatures, but the lower the temperature becomes, the larger this discrepancy

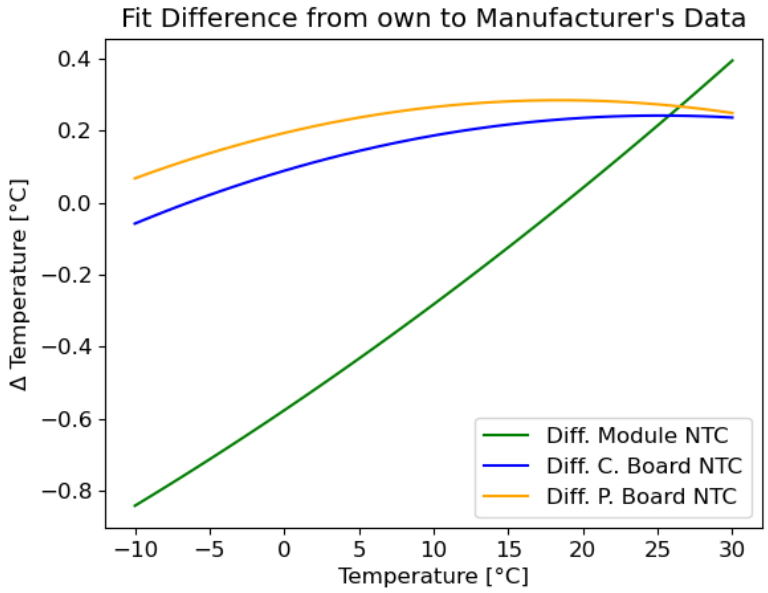

Figure 6.11: Temperature vs. temperature difference between the fit based on the manufacturer's data and the fit applied on the single module NTC (green), connector board (blue), and power board (yellow) NTC climate chamber measurements.

gets. It is clear that the temperature-dependences of the three resistances are not identical to each other.

Temperature [°C]	Interlock Power Board NTC [Ω]	Interlock Connector Board NTC [Ω]	Module NTC [Ω]
30.78 ± 0.03	8009 ± 1 ± 2	8004 ± 0 ± 2	7999 ± 0 ± 2
25.87 ± 0.03	9609 ± 3 ± 2	9594 ± 3 ± 2	9559 ± 1 ± 2
20.85 ± 0.03	11597 ± 2 ± 2	11577 ± 3 ± 2	11623 ± 1 ± 2
15.88 ± 0.04	14076 ± 4 ± 2	14044 ± 4 ± 2	14228 ± 2 ± 2
10.81 ± 0.04	17227 ± 5 ± 3	17173 ± 5 ± 3	17580 ± 2 ± 3
5.83 ± 0.04	21192 ± 8 ± 3	21110 ± 8 ± 3	21761 ± 2 ± 3
0.76 ± 0.03	26327 ± 5 ± 4	26208 ± 6 ± 4	27096 ± 2 ± 4
-4.27 ± 0.04	32817 ± 14 ± 4	32649 ± 14 ± 4	33899 ± 4 ± 4
-9.26 ± 0.03	41105 ± 12 ± 5	40881 ± 12 ± 5	42507 ± 6 ± 5

Table 6.3: Climate chamber measurements for interlock power board, interlock connector board and module NTC. For the temperature the error is statistical and for the resistances the first error is statistical and the second systematic.

The manufacturer's data on the resistance values of the NTCG103JF103FTDS single module NTC for the temperatures measured in the climate chamber can be seen in Table 6.4 with their respective systematic errors. The temperature-dependence of the

NTCG103JF103FTDS is identical to that of the NTCG163JF103FT1S used for the two optobox interlock NTC. If the values are compared to the closest temperature measured in the climate chamber in Table 6.3, the resistances of the three NTCs measured were for the most part within 1σ of the manufacturer's value. The largest discrepancies can be found for the single module NTC at low temperatures, where the discrepancy is in the 2σ interval.

Temperature [°C]	NTCG103JF103FTDS [Ω]
-10	42500± 1000
-9	40570± 970
-5	33930± 760
-4	32460± 710
0	27280± 550
1	26140± 520
5	22070± 400
6	21170± 370
10	17960± 290
11	17250± 270
15	14700± 210
16	14130± 190
20	12090± 150
21	11640± 140
25	10000± 100
26	9630± 100
30	8312± 99
31	8015± 98

Table 6.4: Manufacturer's data on resistance of the NTCG103JF103FTDS for the temperature range of the climate chamber measurements with systematic errors [50].

The climate chamber measurements are in agreement with the manufacturer's data provided for the NTCs used in the OB demonstrator. The fit of the Steinhart-Hart equation is then applied to the manufacturer's data. The first reason for that is that the manufacturer's data provides more statistics than the climate chamber measurements. The second reason is that lower temperatures are included in the manufacturer's data than were achievable in the climate chamber due to sensitive electronics in the optobox and the module chip.
As result of the climate chamber measurement it can be concluded that the three measured NTC agreed well enough with the manufacturer's data to use the three fit parameters of the Steinhart-Hart equation calculated in Eq. 6.4 for all NTC of the types NTCG163JF103FT1S and NTCG103JF103FTDS in the OB demonstrator. However, the

measurement showed that with the single module NTC measured, there are also NTCs that are on the outer boundary of the accuracy guaranteed by the manufacturer, with up to 1 °C difference in temperature to the correct data. If this temperature accuracy is insufficient for the demonstrator setup, further measurements will be needed and fits applied to single NTC based on their own temperature dependence.
As a result of the manufacturer's data being validated for the NTCs, the three parameters of the Steinhart-Hart Eq. 6.4 fitted to the manufacturer's data in Eq. 6.5 are used for the conversion of the NTC resistance into temperature in the WinCC OA project of the OB demonstrator.

7 Conclusion

During my master's thesis I familiarized myself with the DCS of the ITk pixel OB demonstrator and implemented improvements to it.
First, I created panels for single module temperature and voltage monitoring of the LLS. Due to the use of colour spectra associated with the monitored values, the monitoring is intuitive for people using the panel. Local tests of the panels and the implementation in the FSM were successful. The panels are ready for the system tests of the longeron and half-ring SP chains that are in the process of being added to the OB demonstrator.
I also implemented archiving for the OB demonstrator DCS with an Oracle backend for the WinCC OA project on the SR1 DCS PC and an InfluxDB backend for testing sites outside of CERN. In local tests, InfluxDB archiving was successful. The panel I created for bulk addition of data point elements to the database operated without problems. After the update of the Oracle database scheme to 8.20, archiving worked for the SR1 WinCC OA project as well. I made a list of the data point elements to be added to the database and added them to the archive with smoothing configurations chosen for the respective type of data point element. The archiving of all relevant data point elements will be useful for the system tests of the OB demonstrator.
Lastly, I implemented several calibrations for the voltage and temperature monitoring I implemented in the OB demonstrator DCS. The ADC calibration of MOPS chip 10 led to more accurate voltage and temperature monitoring for all modules of the short SP chain on the longeron of the demonstrator. I conducted climate chamber measurements of the optobox temperature monitoring and three NTC resistances. The results were used for an absolute calibration of the optobox temperature monitoring including the uncalibrated ADC of the MOPS chip and a new temperature conversion of its NTCs in the form of a fit to the Steinhart-Hart equation. The climate chamber measurements were also used to validate the manufacturer's data for the three NTCs measured. Then a fit of the Steinhart-Hart equation was applied to manufacturer's data of the temperature-dependence of the resistance of these NTCs. The resulting fit parameters for both the absolute calibration of the optobox MOPS temperature monitoring and the new conversion of the NTC resistances are used in the DCS of the OB demonstrator.

The ITk pixel OB demonstrator will soon have the final number of modules mounted. System tests are taking place in order to validate the demonstrator setup in the final design review phase. The DCS is improved alongside the demonstrator in real world working conditions. Once the final design review is approved, the final ITk pixel detector will be constructed. An optimised DCS is necessary to fully explore the potential of this new detector for the HL-LHC upgrade. This master's thesis aims to contribute to the user-friendliness of the DCS for operators, the archiving of monitored data, and a more accurate monitoring of physical values. An easier operation of the ATLAS experiment for the HL-LHC will lead to fewer operational errors, archived data is needed for evaluation of the detector setup, and more accurate physical monitoring will make the operation safer.

Bibliography

[1] ATLAS Collaboration, *The ATLAS Experiment at the CERN Large Hadron Collider*, JINST **3** (2008) S08003.

[2] L. Evans and P. Bryant, *LHC Machine*, JINST **3** (2008) S08001.

[3] CMS Collaboration, *The CMS experiment at the CERN LHC*, JINST **3** (2008) S08004.

[4] ATLAS Collaboration, *Observation of a new particle in the search for the Standard Model Higgs boson with the ATLAS detector at the LHC*, Phys. Lett. B **716** (2012).

[5] CMS Collaboration, *Observation of a New Boson at a Mass of 125 GeV with the CMS Experiment at the LHC*, Phys. Lett. B **716** (2012).

[6] ATLAS Collaboration, *Technical Design Report for the ATLAS Inner Tracker Pixel Detector*, 2017, URL: `https://cds.cern.ch/record/2285585`.

[7] S. L. Glashow, *Partial-symmetries of weak interactions*, Nucl. Phys. **22** (1961) 579, ISSN: 0029-5582.

[8] A. Salam, W. Svartholm (ed.), *Elementary Particle Physics: Relativistic Groups and Analyticity*, Eighth Nobel Symposium. : Almquvist and Wiksell (1968) 367.

[9] S. Weinberg, *A Model of Leptons*, Phys. Rev. Lett. **19** (21 1967) 1264.

[10] N. Cabibbo, *Unitary Symmetry and Leptonic Decays*, Phys. Rev. Lett. **10** (12 1963) 531.

[11] F. Englert and R. Brout, *Broken Symmetry and the Mass of Gauge Vector Mesons*, Phys. Rev. Lett. **13** (1964) 321.

[12] P. W. Higgs, *Broken Symmetries And The Masses Of Gauge Bosons*, Phys. Rev. Lett. **13** (1964) 508.

[13] G. S. Guralnik et al., *Global Conservation Laws and Massless Particles*, Phys. Rev. Lett. **13** (20 1964) 585.

[14] M. Gell-Mann, *Symmetries of Baryons and Mesons*, Phys. Rev. **125** (3 1962) 1067.

[15] G. Altarelli, *A QCD primer*, AIP Conf. Proc. **631** (2002) 70.

[16] A. B. Arbuzov, *Quantum Field Theory and the Electroweak Standard Model*, (2017) 1.

[17] S. F. Novaes, "Standard model: An Introduction", *Particles and fields. Proceedings, 10th Jorge Andre Swieca Summer School, Sao Paulo, Brazil, February 6-12, 1999*, 1999 5.

[18] J. Goldstone, A. Salam, and S. Weinberg, *Broken Symmetries*, Phys. Rev. **127** (3 1962) 965.

[19] V. C. Rubin, J. Ford, and W. Kent, *Rotation of the Andromeda Nebula from a Spectroscopic Survey of Emission Regions*, Astrophysical Journal **159** (1970).

[20] H. Georgi, H. R. Quinn, and S. Weinberg, *Hierarchy of Interactions in Unified Gauge Theories*, Phys. Rev. Lett. **33** (7 1974) 451.

[21] L. Arnaudon et al., *Linac4 design report*, vol. 6, CERN Yellow Reports: Monographs, Geneva: CERN, 2020.

[22] ATLAS Collaboration, *The ATLAS Inner Detector commissioning and calibration*, Eur. Phys. J. C **70** (2010) 787.

[23] I. Perić et al., *The FEI3 readout chip for the ATLAS pixel detector*, Nucl. Inst. and Meth. A **565** (2006).

[24] A. La Rosa, *The ATLAS Insertable B-Layer: from construction to operation*, JINST **11** (2016) C12036.

[25] M. Garcia-Sciveres et al., *The FE-I4 pixel readout integrated circuit*, Nucl. Inst. and Meth. A **636** (2011) S155.

[26] A. Ahmad et al., *The silicon microstrip sensors of the ATLAS semiconductor tracker*, Nucl. Inst. and Meth. A **578** (2007) 98, ISSN: 0168-9002.

[27] Viaux Maira, N., *The ATLAS New Small Wheel new Muon Stations Ready for LHC Run3*, tech. rep., CERN, 2022.

[28] ATLAS Collaboration, *Operation of the ATLAS trigger system in Run 2*, JINST **15** (2020) P10004.

[29] CERN, *High Luminosity LHC Project*, URL: `https://hilumilhc.web.cern.ch/`.

[30] ATLAS Collaboration, *Expected tracking and related performance with the updated ATLAS Inner Tracker layout at the High-Luminosity LHC*, tech. rep. ATL-PHYS-PUB-2021-024, CERN, 2021, CDS: 2776651.

[31] ATLAS Collaboration, *Technical Design Report for the ATLAS Inner Tracker Strip Detector*, 2017, URL: `https://cds.cern.ch/record/2257755`.

[32] D. Álvarez et. al, *Design Overview of the Bare Local Supports for the ITk Pixel Outer Barrel, Technical Requirements*, tech. rep. AT2-IP-ER-0013, ATLAS Collaboration, 2021, EDMS: 2632352 v.1.

[33] D. Giugni et al., *Specifications for the ATLAS ITk Pixel Services, Technical Requirements*, tech. rep. AT2-IP-EP-0007, version 2, ATLAS Collaboration, 2020, EDMS: 1817540 v.3.

[34] D. Alvarez Feito et al., *On-Detector Services – Outer Barrel, ITk Pixel - Supporting documentation for PDR*, 2020, URL: https://indico.cern.ch/event/881276/.

[35] M. Garcia-Sciveres, *The RD53A Integrated Circuit*, tech. rep. CERN-RD53-PUB-17-001, CERN, 2017, eprint: https://cds.cern.ch/record/2287593/files/RD53A_Manual_V3-51.pdf.

[36] RD53 Collaboration, *RD53B users guide*, tech. rep., CERN, 2020.

[37] P. Dervan, *System Tests for the ATLAS ITk Pixel Detector*, tech. rep., 2021, eprint: http://cds.cern.ch/record/2775693/files/ATL-ITK-SLIDE-2021-326.pdf.

[38] B. Vormwald, *OB Prototype Demonstrator, Status Updates*, 2021, URL: https://indico.cern.ch/event/920306/.

[39] A. Walsemann et al., *A CANopen based prototype chip for the Detector Control System of the ATLAS ITk Pixel Detector*, PoS **TWEPP2019** (2020) 013.

[40] A. Barriuso Poy et al., *The detector control system of the ATLAS experiment*, JINST **3** (2008) P05006.

[41] P. Nikiel, *ELMB128 Documentation*, 2017, eprint: ATL-DQ-ON-0006, URL: https://edms.cern.ch/document/684947/4.5.

[42] O. Holme et al., *The JCOP Framework*, tech. rep., CERN, 2005, eprint: https://cds.cern.ch/record/907906.

[43] *WinCC OA Architecture*, Accessed: 2022-11-06, URL: https://www.winccoa.com/documentation/WinCCOA/3.18/en_US/GettingStarted/GettingStarted-06.html.

[44] R. Kopeliansky, S. Schlenker, *DCS: Requirements Document for HL-LHC*, tech. rep. ATU-GE-ES-0004, ATLAS Collaboration, 2020, EDMS: 2276493 v.1.

[45] M. Ressegotti, *ITk Pixel DCS*, 2022, URL: https://twiki.cern.ch/twiki/bin/viewauth/Atlas/ITkPixelDCS.

[46] N. Lehmann, *Demonstrator DCS*, 2022, URL: https://twiki.cern.ch/twiki/bin/view/Atlas/DemonstratorDCS.

[47] S. Kersten et al., *The Interlock Matrix Crate of the ATLAS IBL detector*, tech. rep. ATL-IP-ES-0203, ATLAS Collaboration, 2021, EDMS: 1302654 v.1.

[48] S. Schäpe, *ITk SR1 CO2 Cooling Plant for Pixel*, 2019, URL: https://twiki.cern.ch/twiki/bin/view/Atlas/ITkSR1CO2PlantPixeloperation.

[49] R. Kulaga, *NextGenArchiver*, 2021, URL: https://edms.cern.ch/document/2397531/1.1.1.

[50] *Manufacturer's Data for the NTC Chips of the NTCG Series*, 2022, URL: https://product.tdk.com/system/files/dam/doc/product/sensor/ntc/chip-ntc-thermistor/catalog/tpd_automotive_ntc-thermistor_ntcg_en.pdf.

[51] *ITk Pixel Hybrid Design*, 2022, URL: https://twiki.cern.ch/twiki/bin/viewauth/Atlas/ITKPixelHybridDesign#BoM.

[52] S. G. Sevilla, *ADC Count Measurements of MOPS Chips*, 2022, URL: https://docs.google.com/spreadsheets/d/1vqXIshUKESwOEJZvWbvAoPukgosprbj5Pg69-93S_aE/edit#gid=831029934.

[53] *Characteristics Keithley 2000 Multimeter*, 2022, URL: https://aisdb.cern.ch/pls/htmldb_aisdb_prod/f?p=189:14:13759459343972::::P14_PDF:2683.

[54] *Data Sheet bPOL12V$_V$6Converter*, 2022, URL: https://espace.cern.ch/project-DCDC-new/Shared%5C%20Documents/bPOL12V%5C_V6%5C%20datasheet%5C%20V1.5.pdf.

[55] C. Chen et al, *A gigabit transceiver for the ATLAS inner tracker pixel detector readout upgrade*, JINST **14** (2019) C07005.

Danksagung

A year of work went into these pages and while I am very happy to be finally finished, I had quite a good time. This is thanks to all the people that made this possible for me.
I want to thank Stan, a professor that I bragged about quite regularly to other students for the time and efforts he dedicates to the people in his working group. You are a great supervisor and person to work with. I also want to thank Hans and Benedikt, without whom I would have felt really lost in the joys of linking panels in WinCC and concussive maintenance of the climate chamber. Thank you for all the time you took to help me install the necessary programs, explain how the demonstrator and its DCS work, and in general support me in my research.
Lastly I want to thank my mother and my brother. Mama, Felix, ihr habt nie aufgehört an mich zu glauben und ich freue mich schon darauf, mit euch meinen Master zu feiern!

Erklärung nach §17(9) der Prüfungsordnung für den Bachelor-Studiengang Physik und den Master-Studiengang Physik an der Universität Göttingen:
Hiermit erkläre ich, dass ich diese Abschlussarbeit selbständig verfasst habe, keine anderen als die angegebenen Quellen und Hilfsmittel benutzt habe und alle Stellen, die wörtlich oder sinngemäß aus veröffentlichten Schriften entnommen wurden, als solche kenntlich gemacht habe.
Darüberhinaus erkläre ich, dass diese Abschlussarbeit nicht, auch nicht auszugsweise, im Rahmen einer nichtbestandenen Prüfung an dieser oder einer anderen Hochschule eingereicht wurde.

Göttingen, den 16. Februar 2023

(Anne Gaa)